



Royal Netherlands
Meteorological Institute
Ministry of Infrastructure
and Water Management

The EUMETSAT
Network of
Satellite
Application
Facilities



OSI SAF
Ocean and Sea Ice



EUMETSAT
NWP SAF
NUMERICAL WEATHER PREDICTION



EUMETSAT

Ocean and Sea Ice SAF / NWP SAF

CFOSAT and WindRad Rotating Fan-beam SCATterometer Simulation and Wind Retrieval Performance Evaluation

SAF/OSI/CDOP3/KNMI/TEC/TN/348

NWPSAF-KN-TR-029

29 July 2019

Zhen Li, Ad Stoffelen, Anton Verhoef

*Royal Netherlands Meteorological Institute (KNMI)
De Bilt, the Netherlands*

DOCUMENTATION CHANGE RECORD

References: SAF/OSI/KNMI/TEC/TN/348

NWPSAF-KN-TR-029

Issue / Revision :	Date :	Change :	Description :
Version 0.1	2017-06-28		1 st draft by Zhen Li
Version 0.2	2018-02-02	add	Combine CFOSAT SCAT/WindRad
Version 0.3	2019-07-29	add	Align with AMT manuscript

CFOSAT and WindRad Rotating Fan-beam SCATterometer Simulation and Wind Retrieval Performance Evaluation

Zhen Li, Ad Stoffelen, Anton Verhoef

KNMI, the Netherlands

Contents

1. Introduction.....	4
1.1 CFOSAT.....	4
1.2 WindRad	5
2. RFSCAT concept.....	6
3. Generic simulation system for rotating scatterometer	9
3.1 L1B data simulation and L2A data aggregation	9
3.2 Simulation model validation	13
3.3 Geometry distribution	14
3.3 Instrument noise.....	17
4. Wind inversion	20
4.1 Bayesian approach	20
4.2 Wind retrieval performance evaluation.....	24
4.2.1 Assessments with the input wind field.....	24
4.2.2 Figures of Merit	28
4.2.3 Wind direction bias	32
4.3 Wind direction skill optimization.....	34
4.3.1 Beam weighting method	34
4.3.2 Beam weighting various settings and comparison.....	37
5. Conclusion	46
References.....	49

1. Introduction

It has been proven that wind scatterometers are efficient and powerful for measuring global sea surface wind fields. Space borne wind observations are important for a wide range of applications, such as now-casting, short-range forecasting and global and mesoscale numerical weather prediction (NWP) through NWP data assimilation. The primary mission of a wind scatterometer is to obtain wind speed and wind direction over the ocean from backscatter measurements. It is achieved by performing inversion over a set of backscatter measurements at various geometries in the Wind Vector Cell (WVC) through a Geophysical Model Function (GMF).

For static fan-beam scatterometers and rotating pencil-beam scatterometers wind retrieval has been well elaborated employing different solutions to deal with the non-linear GMF, the sparse azimuth sampling and the ambiguous wind vector solutions [1][2]. Two new types of scatterometer: 1) a Ku-band rotating fan-beam scatterometer (RFSCAT) called CFOSAT (launched on 29th Oct 2018), and 2) a dual (Ku and C bands) frequency RFSCAT, called WindRad (planned to launch in 2019), as described in this report. The report addresses RFSCAT simulation and wind retrieval performance evaluation for both CFOSAT and WindRad. A generalized simulation has been built to compare the wind retrieval performance of rotating beams between RFSCAT and Pencil-beam (with SCAT, WindRad and SeaWinds as examples) which is described in the peer reviewed paper [3].

1.1 CFOSAT

CFOSAT is a joint mission of the Chinese (CNSA) and French (CNES) space agencies and stands for China-France Oceanography SATellite. It is launched in 29th Oct 2018. The goal of the mission is to monitor the ocean surface wind and waves together and to provide data for ocean and atmosphere interaction science in order to improve forecasts for marine meteorology and to increase our knowledge its climate variability. There are two main instruments on board CFOSAT: SCAT (a Ku-band

wind scatterometer supplied by CNSA) and SWIM (a wave scatterometer supplied by CNES). SCAT is the first RFSCAT and operates with alternating horizontal (HH) and vertical (VV) co-polarization to obtain global ocean vector wind observations. From the first scatterometer SEASAT-A Scatterometer System (SASS) to the latest scatterometer on board Scatsat-1 from the Indian Space Research Organization (ISRO), currently all the operational scatterometers can be classified into two types, i.e., multiple fan-beam scatterometers (ASCAT, ERS) with fixed azimuth angle [4] and rotating pencil-beam scatterometers (OSCAT, QuikSCAT) with fixed incidence angle [5]. The advantage of the new concept RFSCAT as compared to current existing types is the combined feature of a fan beam rotation. The antenna beam sweeps the earth surface similar like the pencil beam, but with a much larger range of incidence angles from 25 to 47 degree and wide swath of 1000 km. Large overlaps of the sweep can be produced with the spacecraft speed around 6.7 km/s and the 3.3 rpm rotating speed of the beam [6]. The large overlaps enable up to 18 different geometrical views in one WVC with diverse azimuth angle. This feature is able to significantly improve the wind retrieval performance in most of the swath as further discussed later on.

1.2 WindRad

WindRad on the Feng Yun-3E (FY-3E) meteorological satellite is being developed in China. The FY-3 series of satellites are the second-generation polar-orbiting meteorological satellites, and they will be located in three sun-synchronous orbital planes. The four main capabilities of the FY-3 satellites are atmospheric temperature sounding, atmospheric humidity sounding, greenhouse gas detection and OVW (Ocean Vector Winds) at high precision. WindRad also adopts the RFSCAT concept, and the main difference comparing to SCAT is the dual frequency radar (C-band and Ku-band) with four beams. Accurate wind field measurements are expected to be achieved and its OVW data will significantly contribute to improve weather forecast. There are three main objectives for WindRad: 10-km spatial resolution, high-wind retrieval capability, near all-weather capability (especially the effect of rain).

2. RFSCAT concept

The working principle of the RFSCAT on SCAT and WindRad are shown in Figure 1 and Figure 2. The satellite goes along the track and the fan beam antenna rotates at the same time such that its footprint sweeps a wide donut shape on the earth surface. Large overlaps can be produced by the successive sweeps. The radar operates in a pulsed mode, so that each point of the echo profile is able to be assigned to a unique pixel within the antenna footprint along the radial direction. SCAT operates in Ku-band VV and HH polarization in turns. For WindRad, the C-band and Ku-band antennas sit oppositely on the spinning platform, and both of them transmit and receive VV and HH polarizations in turns.

The swath is divided into WVCs and each WVC within the swath is intercepted by the antenna footprint at a number of times depending on the position in the swath. Figure 3 illustrates how the scanned antenna footprint and WVCs in the swath interfere with each other. The sweet swath (located in between the edge of the swath and the nadir swath) is the region with the most interceptions per WVC, while the outer and nadir swaths contain much less. The sweet swath has diverse azimuth angles and multiple views. The outer swath is only illuminated at large incidence angles with azimuth angles limited to some range around 90° or -90° w.r.t. flying direction. The nadir swath is only observed in a narrow range around two opposite azimuth directions, i.e., 0° and -180° w.r.t. the flying direction. The wind direction accuracy depends on the diversity of the observation geometry. The limited diversity of the azimuth angles in the outer and nadir swath implies that the wind direction ambiguities are most likely to be ill defined and skew, while the best quality is achieved in the sweet swath.

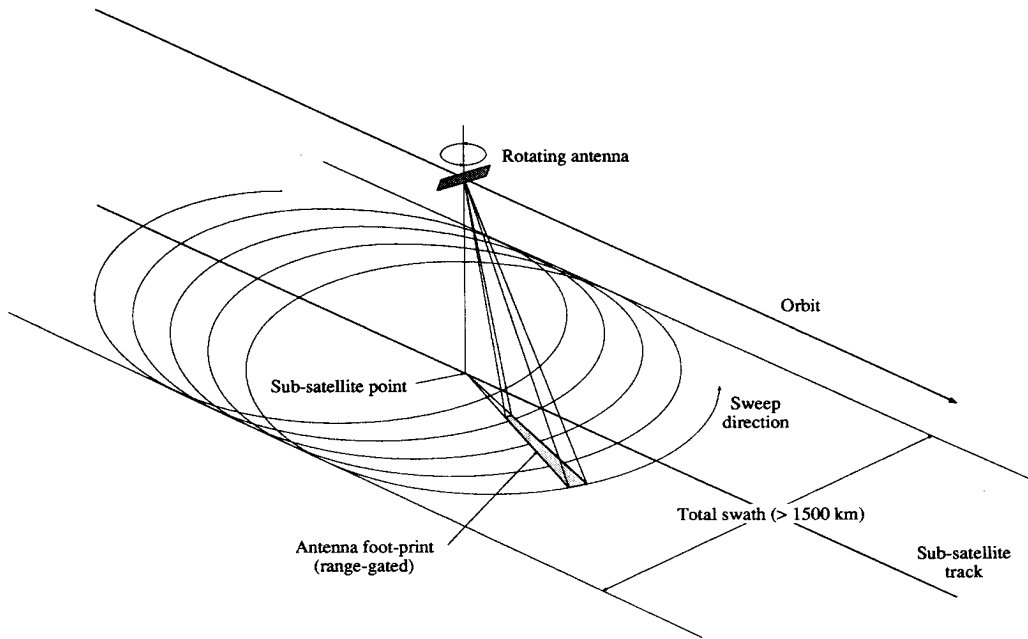


Figure 1 Rotating fan beam for CFOSAT [7].

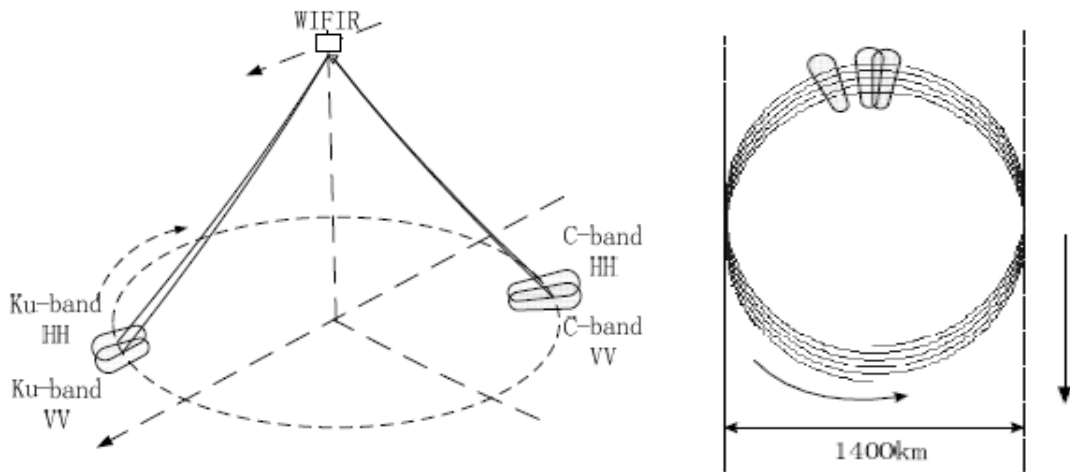


Figure 2 Rotating fan beam for WindRad [8] in 3D (left) and on the earth's surface (right).

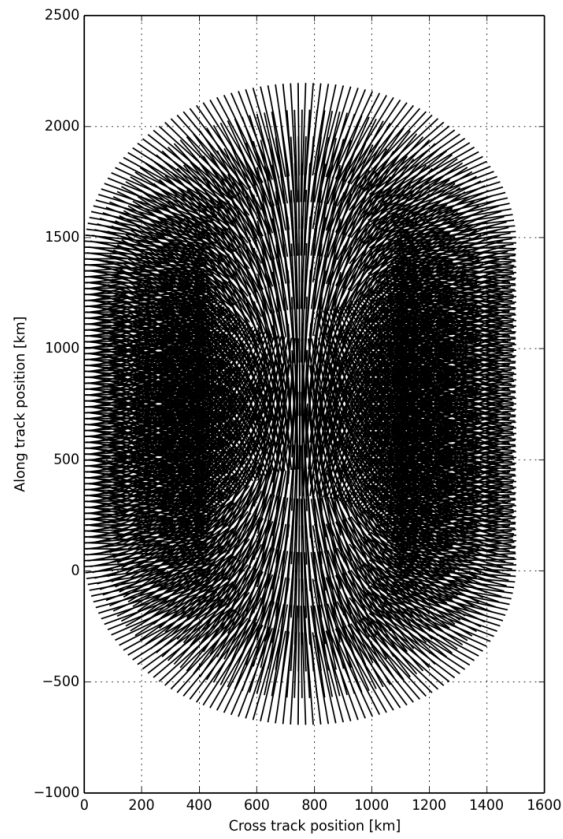


Figure 3 Illustration of scanned antenna footprint on the ground track over a short time period (3.5 minutes), with almost complete sampling in the middle.

3. Generic simulation system for rotating scatterometers

3.1 L1B data simulation and L2A data aggregation

The simulation is designed to be generic and able to adapt to all of the current rotating-beam wind scatterometers, i.e., both fan beam and pencil beam. It consists of four components: (1) generate satellite state vectors by the orbit propagator SGP4 (Simplified perturbations models) [9]; (2) simulate Normalized Radar Cross Section (NRCS) data; (3) assign the NRCS data onto the proper WVCs (L1B product); (4) aggregate L1B data in one WVC into views (L2A product). The work flow charts are shown in Figure 4 and Figure 5. The instrument and processing parameters for SCAT and WindRad are shown in Table 1 and Table 2. The simulation of rotating pencil-beam (SeaWinds) has also been done in our study in order to compare with RFSCAT system (Table 3). We use ECMWF model wind as input wind field to initialize the L1B simulation, which provides a spatially smooth ocean wind truth. To represent the sampling of local wind variability (turbulence) near a WVC, geophysical noise is added by disturbing the input wind components u and v assigned on each slice by injecting Gaussian distributed noise. Together with the instrument configurations and satellite state vectors, the observation geometries on slice level are calculated. The instrument noise K_{pc} is estimated by $K_{pc}^2 = A + \frac{B}{SNR} + \frac{C}{SNR^2}$. However, the coefficients A , B , and C need onboard processing details, which are not the same nor available for all scatterometers. In order to make the simulator generic, A , B , and C for each slice are calculated by $A = \frac{1}{B_s \times t_d}$, $B = \frac{2}{B_s \times t_r}$, $C = \frac{1}{B_s \times t_r}$, where B_s is the bandwidth for each individual slice, t_d is the transmit duration time, t_r is the receiving time. The distribution of B_s on each slice in one pulse is assigned according to the antenna gain pattern of the pulse.

An example of the simulated satellite orbit together with the location of the slices is given in Figure 6. The NRCS (σ^0) is derived using the NSCAT-4 GMF [10] for Ku-band and the CMOD5n GMF for C-band [11] and the corresponding beam

geometries. Subsequently, the L1B data are obtained after adding the instrument noise on the ‘true’ σ° . The instrument noise is added by multiplying a Gaussian random number in this way: $\sigma^\circ_{noisy} = \sigma^\circ \times (1 + K_{pc} \times Gaussian_random_nr)$. The L1B data are assigned to the proper WVCs [12] and then aggregated into views. A view is a group of slices with similar azimuth angle and the same polarization in one WVC, the properties (i.e. incidence angle, azimuth angle, latitude, longitude, etc.) on the corresponding slices are also aggregated to represent the view [13]. We note that the simulation does currently not include rain effect.

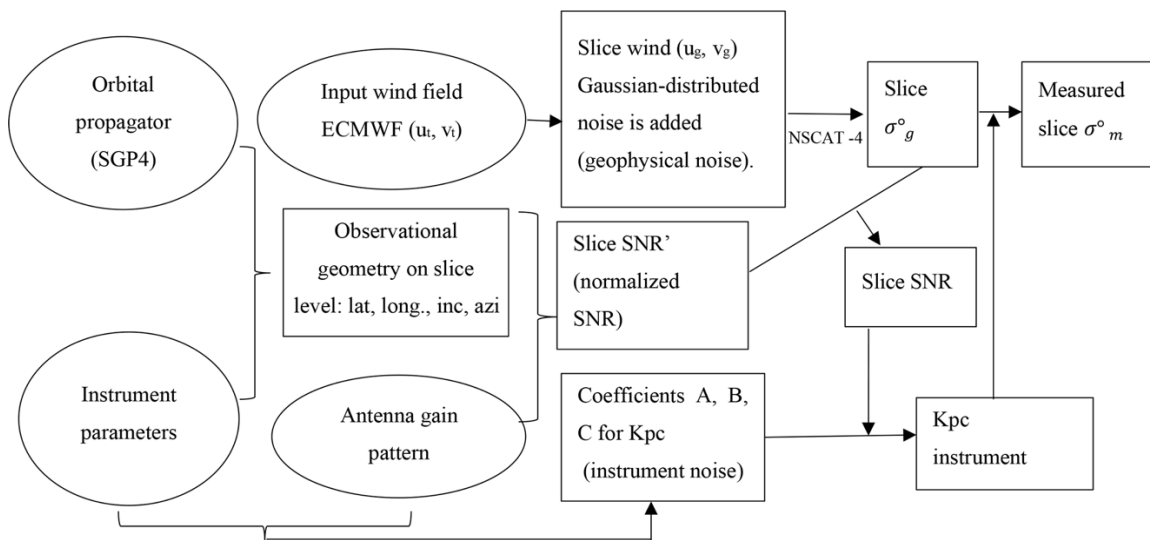


Figure 4 Workflow for the L1B data simulation.

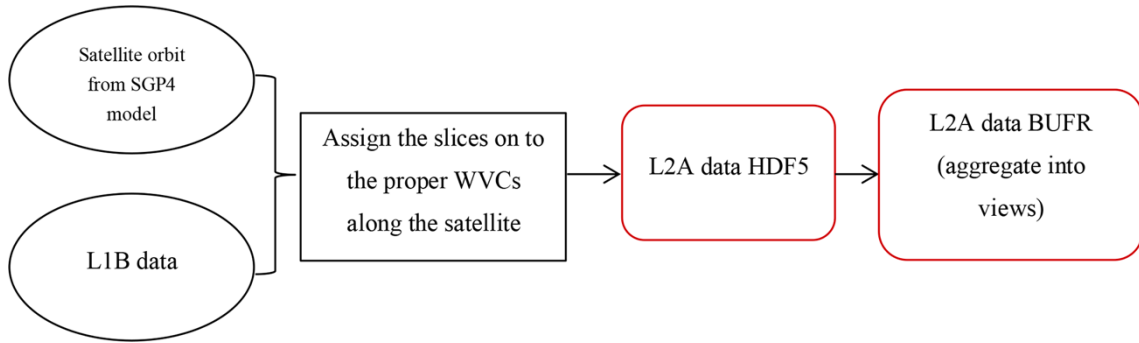


Figure 5 Workflow to assign L1B data to the proper WVCs and aggregate into views.

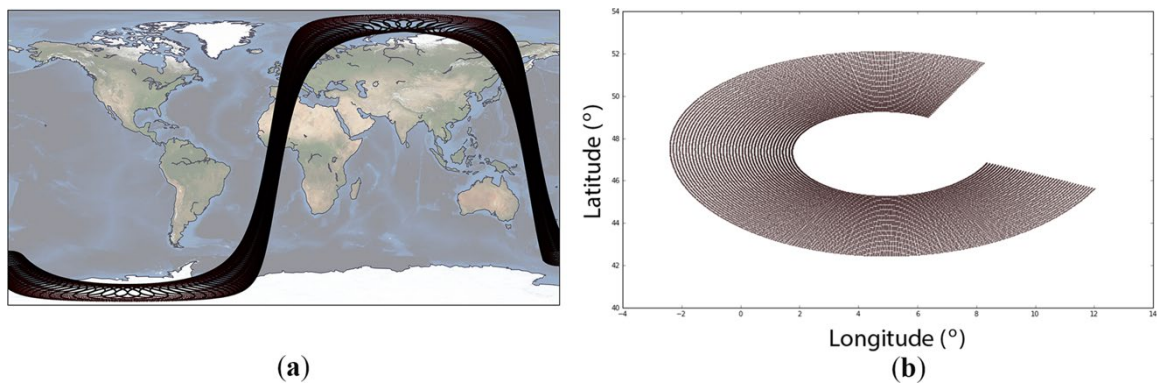


Figure 6: (a) One simulated satellite orbit for CFOSAT starting from 11-12-2011 with the circular motion of the slice located at the end of each pulse; (b) the zoomed in location of all slices on the earth.

Table 1. SCAT input parameters for PLIB simulator

Parameters	Value
Orbit height	514 km
Swath	1000 km
Footprint	280 km
Satellite speed	7.1 km/s
Antenna rotating speed	3.5 rpm
Polarization	VV and HH alternating
Incidence angle range	25 – 48 deg
Antenna pointing angle	40 deg
Peak transmit power	120 W
WVC resolution	25 km
Center frequency	13.256 GHz (Ku-band)
Duration of transmit pulse	1.3 ms
Duration of receiving pulse	2.7 ms
Pulse Repetition Frequency (PRF)	75 Hz
Two-way -3dB beam width (azimuth)	1.28 deg
Peak antenna gain	30 dB
Transmit bandwidth	0.5 MHz

Table 2. WindRad input parameters for PLIB simulator

Parameters	Value	
	Ku-band	C-band
Orbit height		836 km
Swath		1400 km
Footprint		200 km
Satellite speed		7.4 km/s
Antenna rotating speed		3.0 rpm
Polarization	VV and HH alternating	
Incidence angle range	34.7 – 44.5 deg	
Antenna pointing angle	34.8 deg	
WVC resolution	25 km	
Peak transmit power	120 W	100 W
Center frequency	13.256 GHz	5.4 GHz
Duration of transmit pulse	1.8 ms	1.7 ms
Duration of receiving pulse	1.25 ms	1 ms
Pulse Repetition Frequency (PRF)	208 Hz	104 Hz
Two-way -3dB azimuth beam width	1.3 deg	0.52 deg
Peak antenna gain	37 dB	32 dB
Transmit bandwidth	0.6 MHz	

Table 3 QuikScat SeaWinds input parameters for PL1B simulator

Parameters	Value (inner and outer beam)
Orbit height	800 km
Swath	1800 km
Footprint	36 km
Satellite speed	7.0 km/s
Antenna rotating speed	18 rpm
Polarization	VV and HH
Incidence angle range	51.8 deg and 46.7 deg
Antenna pointing angle	44.9 deg and 38.9 deg
Peak transmit power	120 W
WVC resolution	25 km / 12.5 km
Center frequency	13.256 GHz (Ku-band)
Duration of transmit pulse	1.5 ms
Duration of receiving pulse	2.1 ms
Pulse Repetition Frequency (PRF)	96 Hz
Two-way -3dB beam width (azimuth)	1.8 deg
Peak antenna gain	38 dB
Transmit bandwidth	0.375 MHz

3.2 Simulation model validation

The performance of the scatterometer simulator on actual wind field is a good means to establish the validity of the simulation model. SeaWinds is chosen to compare real data with simulated data because it is the only scatterometer for which real data are available among the three scatterometers here. In total 14 orbits (one day) of data are included in the validation. The maximum collocation distance between real and simulated data points is set to 10 km and the number of collocated data is 75867 and Figure 7 shows the collocated wind retrieval result. The simulated wind speed and wind direction give a good correlation against to the real SeaWinds data, which means the simulation model has a good performance as expected to the real scatterometer, and it is suitable for the comparison among the different type of scatterometers.

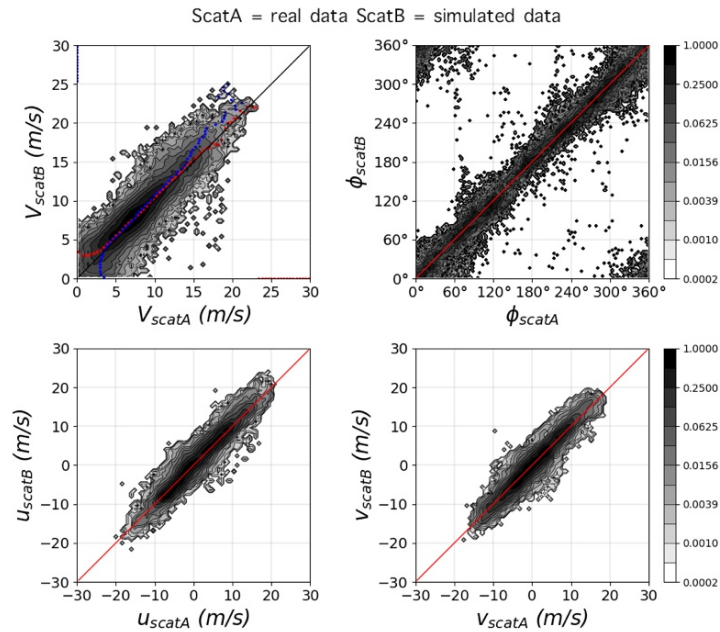


Figure 7 The collocation between SeaWinds (ScatA) and simulated SeaWinds (ScatB) in wind speed (upper left: red points are the average value as a function of wind speed of ScatA; blue points are the average value as a function of wind speed of ScatB), wind direction (upper right), u component (lower left), v component (lower right).

3.3 Geometry distribution

Figure 8 is the average number of views for each WVC column. The slight asymmetry between the left side and right side is caused by the added-up velocity of the rotating antenna and satellite motion, which is different left and right. The most important differences between SCAT, WindRad, and SeaWinds are the shape of the antenna and the number of antennas, directly leading to a different distribution of the number of views across the swath. The number of slices in each view varies across the swath though. For rotating fan-beam instruments, the view number varies across the swath with the feature of less views in the outer and nadir swath, and more views in the parts of the swath in between (Figure 8). SeaWinds as rotating pencil-beam instrument has 4 views in each WVC across the swath, where the fore and aft views in the outer swath are each split in two views. It can be observed that both SCAT and WindRad contain more views than SeaWinds for all WVCs, with a saddle shape in the view count. Moreover, the number of views of WindRad is about twice the number of views of SCAT.

SCAT has up to 18 views at sweet-swath WVC 11 and 28, while WindRad has up to 25 views at sweet-swath WVC 7 and 48 for Ku-band (C-band has the same number due to the same geometry setting). Comparing to SCAT, WindRad's sweet WVCs are not exactly in the middle between the edge and nadir of the swath, and the number of views in the nadir swath is close to this number in the outer swath region, because the length of the footprint is much shorter than that of SCAT.

The analysis of the incident and azimuth view angles as a function of WVC position is performed for every WVC. Here, only the left side of the swath is shown, since both sides are very similar. Incidence and azimuth angles change gradually from outer to nadir swath. Selected WVCs represent the outer, sweet and nadir swath for SCAT and WindRad (Figure 9 and Figure 10). The selected WVC number 11 of SCAT contains the most views, but also need to note that this WVC locates around the inner end of a footprint, where minimum incidence angle occurs, so the incidence angle distribution contains more incidence angles at 25deg and 26 deg. The same reason applies to WindRad WVC number 7, which it also has a larger number of low incidence angle distribution. Both nadir WVCs of SCAT and WindRad have larger number of low and high incidence angle. This is because the low or high incidence angles only occur at the two ends of a footprint and the two ends of a footprint both fall in nadir WVCs, so for the views only contain a few samples from the two ends of a footprint will lead to a low or high incidence angle and it happens often in nadir WVCs. For both wind scatterometers, the incidence angles are relatively evenly distributed at the nadir WVC because the entire footprint is able to sweep over those WVCs, while the azimuth angle range is limited and concentrated around 0 and -180 degrees. As the WVC position moves to the outer swath, the incidence angles are less even and is limited to the highest incidence angles at the outer WVC, while the azimuth angles are the most diverse at the sweet WVCs and limited to a range around -90 degree at the outer WVC. In conclusion, the intermediate swath positions of SCAT and the positions a bit closer to the outer swath of WindRad have the most optimum measurement conditions. The definition of the sweet swath for RFSCAT is therefore not always centered between nadir and outer swath, but determined by the geometry of the rotating beam.

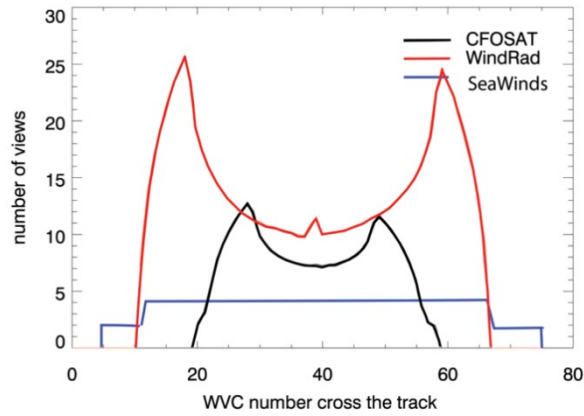


Figure 8 Averaged number of views at the WVCs across the swath.

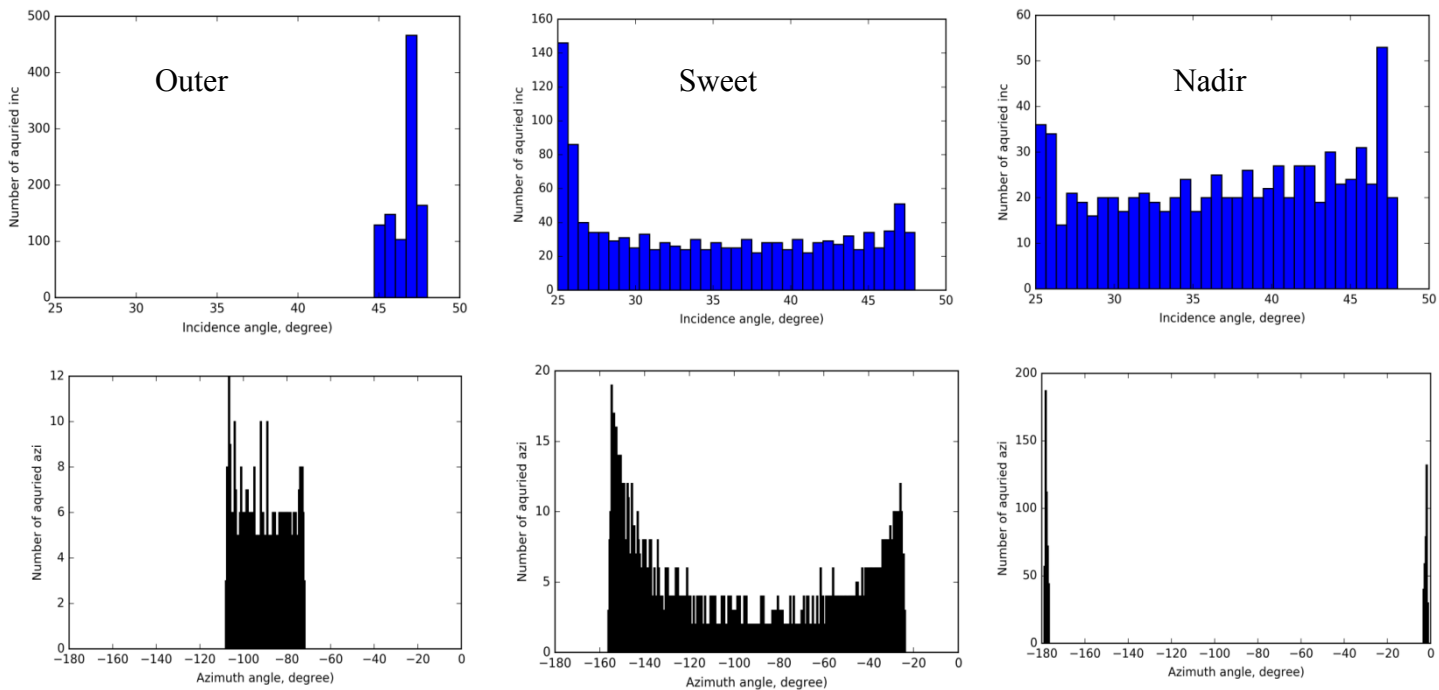


Figure 9 SCAT: incident angle (upper) and azimuth angle (lower) distribution for outer (WVC 0), sweet (WVC 11), nadir (WVC 19).

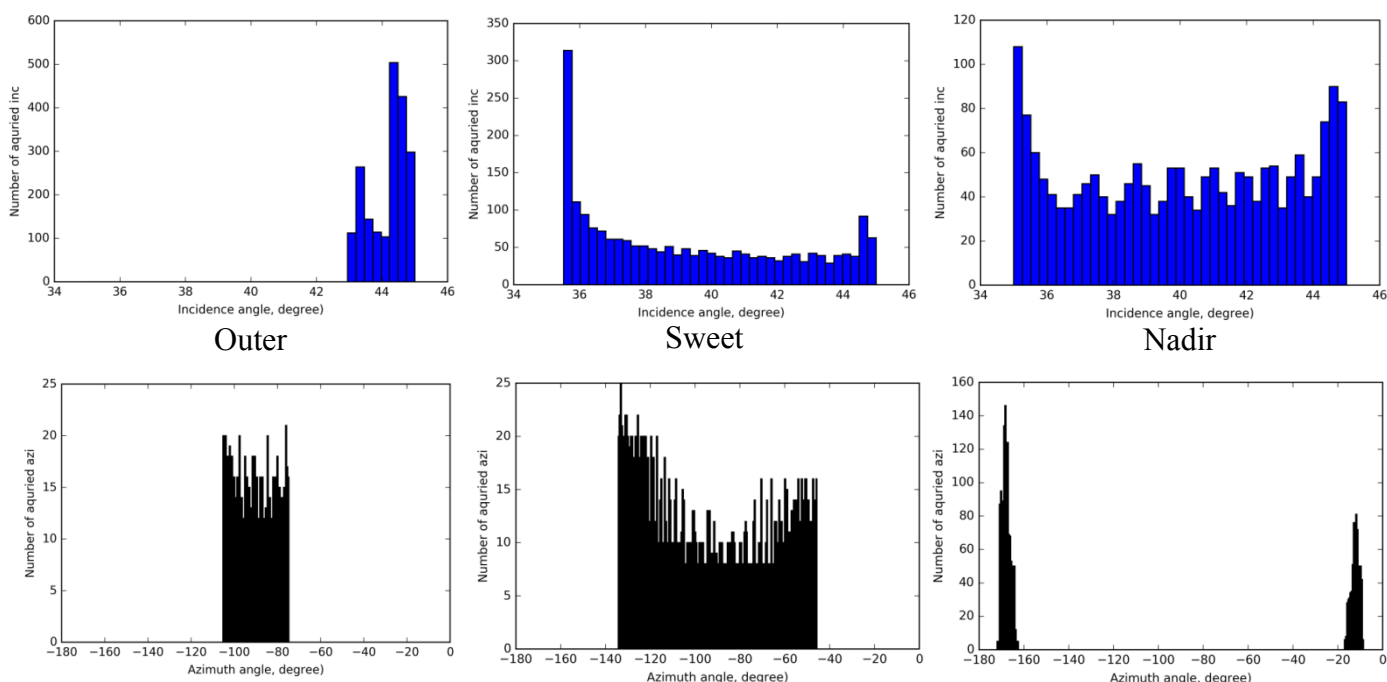


Figure 10 WindRad: incidence angle (upper) and azimuth angle (lower) distribution for outer (WVC 0), sweet (WVC 7), nadir (WVC 22).

3.3 Instrument noise

In the simulator the instrument noise (Kpc) of SCAT, WindRad and SeaWinds are estimated at various wind speeds (4 m/s, 9 m/s, and 16 m/s) on slice level, view level and WVC level. The Kpc for each view is aggregated by weighting the Kpc of the slices in this view and the Kpc on WVC level is derived by averaging the Kpc for all the views in the corresponding WVC, assuming that the WVC wind retrieval performance depends on all views.

Figure 11 (a) shows the slice Kpc of SCAT as a function of incidence angle. The slices with low wind speed and high incidence angle contain high Kpc and Kpc for VV polarization overall is lower than for HH, except for the slices with incidence angle lower than 30.25° (indicated by the dashed line in Figure 11 a). The Kpc in a WVC for SCAT (Figure 11 (b)) is much lower than the Kpc on slice level, as expected due to the aggregation of the slices in a WVC. The outer swath contains relatively high instrument noise as compared to sweet and nadir swath. Low wind speed leads to a higher Kpc. On WVC level, the instrument noise is lower than 20%, except for low wind speed.

WindRad has two frequencies at Ku and C band. As illustrated in Figure 12 (a) and (b), the VV K_{pc} is lower than the HH K_{pc} for Ku and C band and the C-band K_{pc} is much lower than the Ku-band K_{pc}. On the WVC level (Figure 12 (c)), it shows a similar pattern to SCAT and generally the instrument noise is lower than 10% if the outer swath and low wind speeds are excluded.

The SeaWinds K_{pc} on slice level (Figure 13 (a) (b)) is more constant at wind speed of 9m/s and 16m/s, while it is increasing along with the incidence angle at low wind speed 4m/s. On WVC level, the K_{pc} is lower than 20% except for wind speeds below 4m/s. We note that a random error of 20% at 4 m/s is still acceptable in terms of absolute random wind error after wind retrieval.

In general, low wind speeds cause high instrument noise, as expected, and the instrument noise on WVC level is less than 20% for SCAT and less than 10% for WindRad, when the outer swath and low wind speeds are excluded. Both scatterometers above have a pattern of higher K_{pc} at the outer swath as compared to the other parts of the swath.

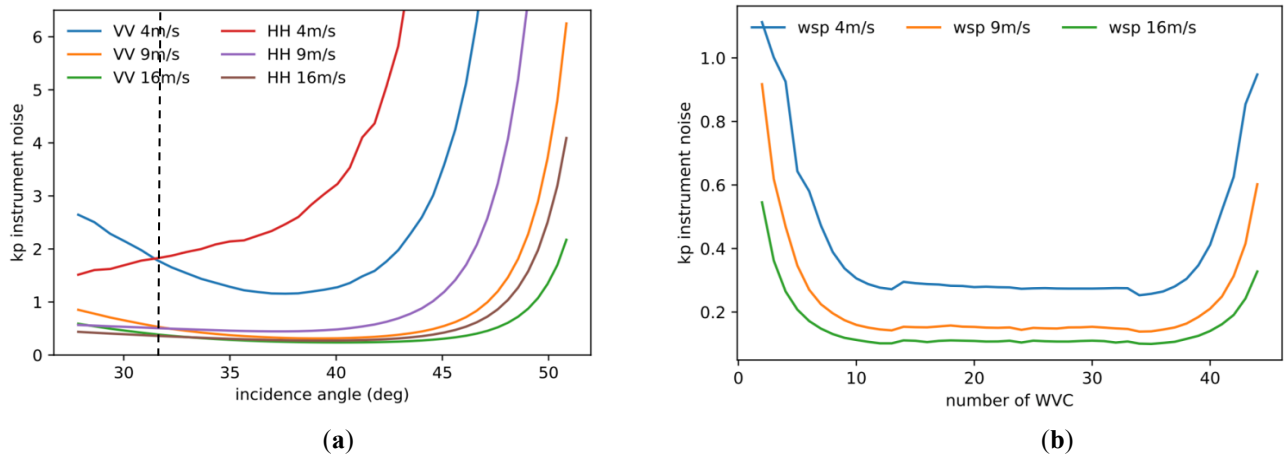


Figure 11 SCAT Kp noise (%) at 4m/s, 9m/s, and 16 m/s on (a) slice level and (b) WVC.

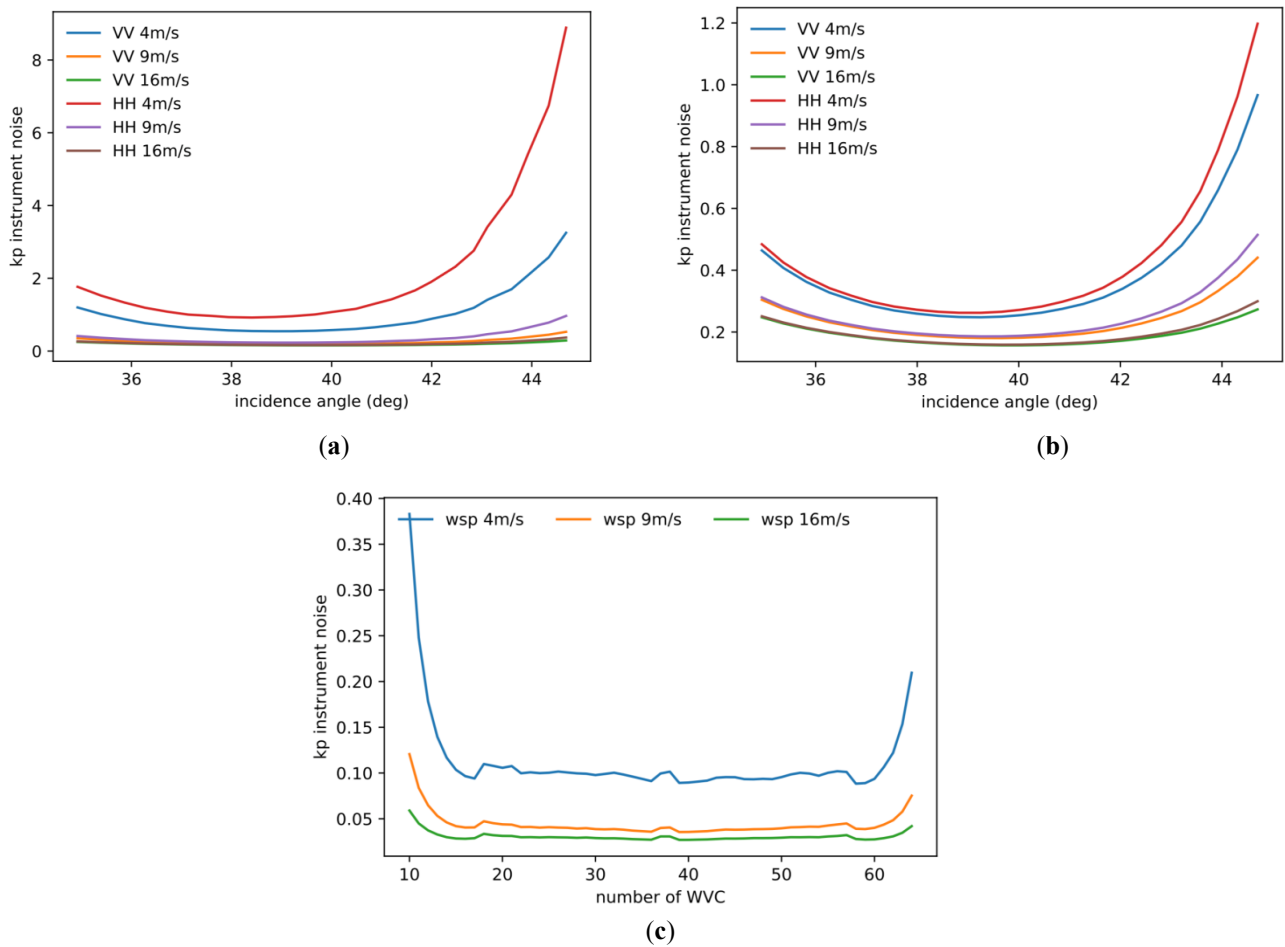


Figure 12 WindRad instrument noise in ratio (1 is 100%) at 4m/s, 9m/s, and 16 m/s on (a) slice level of Ku-band; (b) slice level of C-band (slices with SNR < 0.05 are excluded); (c) WVC mean Kp.

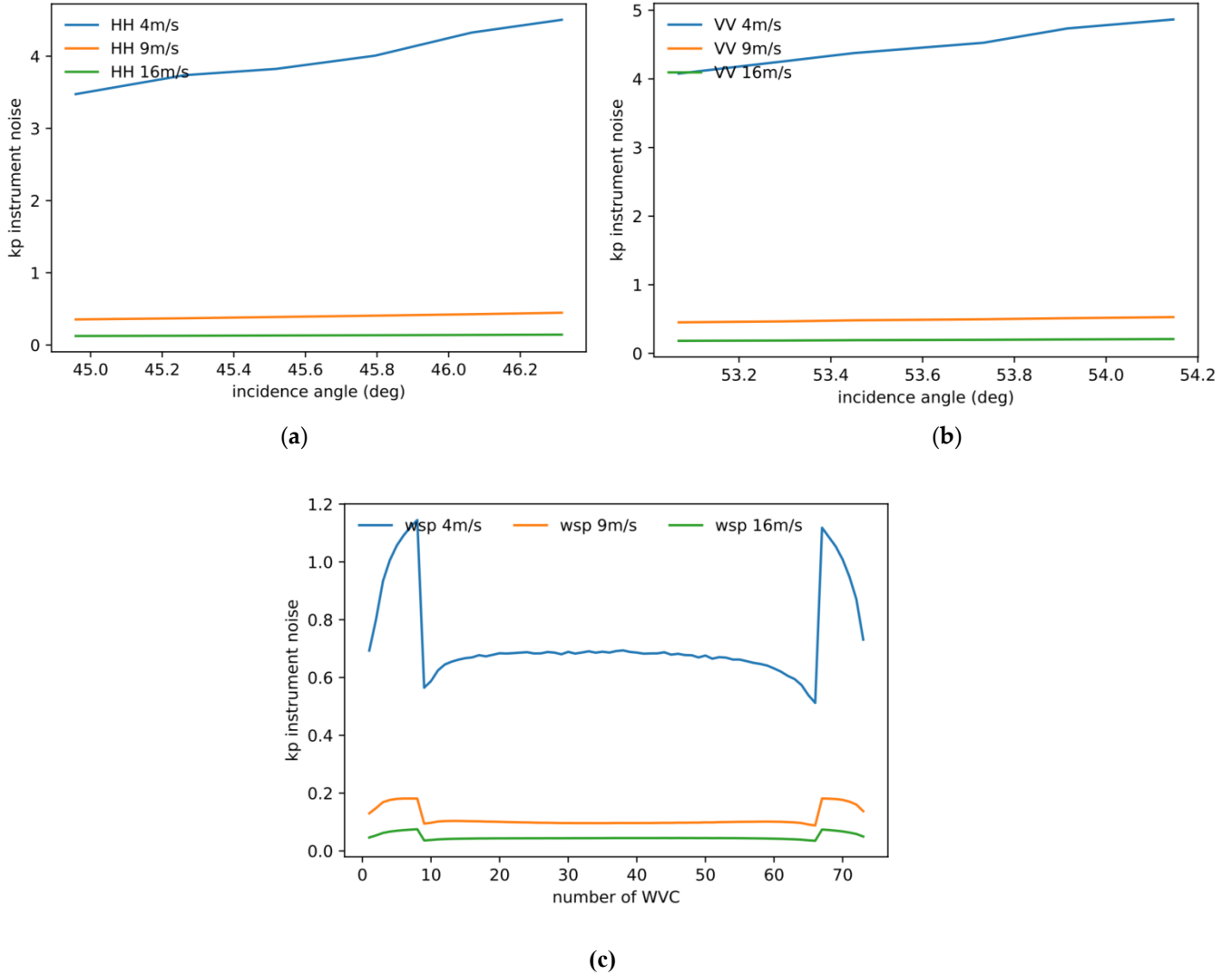


Figure 13 SeaWinds instrument noise in ratio (1 is 100%) at 4m/s, 9m/s, and 16 m/s on (a) slice level of Ku-band HH pol; (b) slice level of Ku-band VV pol (slices with SNR < 0.05 are excluded); (c) WVC mean Kp.

4. Wind inversion

4.1 Bayesian approach

The Bayesian theorem for wind scatterometer states that the probability of σ_s° , given a set of backscatter measurements, is proportional to the probability of this set of backscatter measurements given σ_s° multiplied by the prior probability of σ_s° .

$$P(\sigma_s^\circ | \sigma_{measured}^\circ) = P(\sigma_{measured}^\circ | \sigma_s^\circ) \cdot P(\sigma_s^\circ)$$

Assuming $P(\sigma^{\circ}_s)$ is constant, maximizing $P(\sigma^{\circ}_s|\sigma^{\circ}_{measured})$ by varying σ°_s on the surface of the measurement space manifold, results in only one variable measurement error term $P(\sigma^{\circ}_{measured}|\sigma^{\circ}_s)$ and it can be expanded as the MLE (Maximum Likelihood Estimator) [14][15][1].

$$MLE = \sum_{views} \frac{(\sigma^{\circ}_{measured} - \sigma^{\circ}_s)^2}{(k_p \sigma^{\circ}_{xi})^2} \quad (1)$$

where $\sigma^{\circ}_{measured}$ denotes the measured σ° of each view for the WVC and σ°_s is the simulated σ° , σ°_x is either measured σ° or simulated σ° . MLE is searching for minimum distances between backscatter measurements and backscatter model solutions lying on the empirical GMF surface.

For the equation of MLE, three assumptions are made:

1. Measurement errors are uncorrelated;
2. Their errors are Gaussian;
3. The priori probability $P(\sigma^{\circ}_s)$ is constant.

The third assumption is usually not achieved [16], which leads to a biased wind direction retrieval at some wind directions and WVCs.

The σ°_s with the minimum MLE is known as the first rank solution. However, the highest-ranked solution is often not the best solution because the wind retrieval results usually consist of a set of ambiguous solutions, due to the combination of measurement geometry, the harmonic modulation of the GMF (non-linear GMF), noise, etc. After the wind retrieval step, one of the ambiguous solutions is selected by the Two-Dimensional Variational Ambiguity Removal (2DVAR) [17] after minimizing a total cost function that combines both observational and NWP background contributions and their estimated error structure. The retrieved wind field is used to select the closest ambiguity to the wind field at each WVC.

A statistical comparison of 1st rank solution and 2DVAR performances of SCAT, WindRad and SeaWinds are shown in Figure 14, Figure 15 and Figure 16. For SCAT, the 1st rank solution wind field (Figure 14 (a)) shows poor retrieval quality in the nadir and outer swath, while 2DVAR (Figure 14 (b)) effectively improves the retrieval results here; a similar improvement occurs for SeaWinds (Figure 16). The nadir swath of WindRad shows worse wind retrieval quality than the other parts of the swath (Figure 15 (a)) and 2DVAR is able to correct the false solutions appearing in the 1st

rank solutions. Note that the rotation sampling pattern of WindRad is visible as regular disturbances along the swath. This implies that for the same WVC number, different sets of views are collected, depending on the phase of the antenna rotation, hence the wind retrieval performance may vary, e.g., the expected MLE. One aspect needs to be noted: the 2DVAR with MSS works properly in our simulation, but the input wind field of the simulation is ECMWF model data, which is consistent with the 2DVAR background field. Even though a Gaussian-distributed geophysical noise has been added in the input wind field, it still might lead to a selection of wind solutions that tends to be close to the model wind field and hence somewhat overestimates performance.

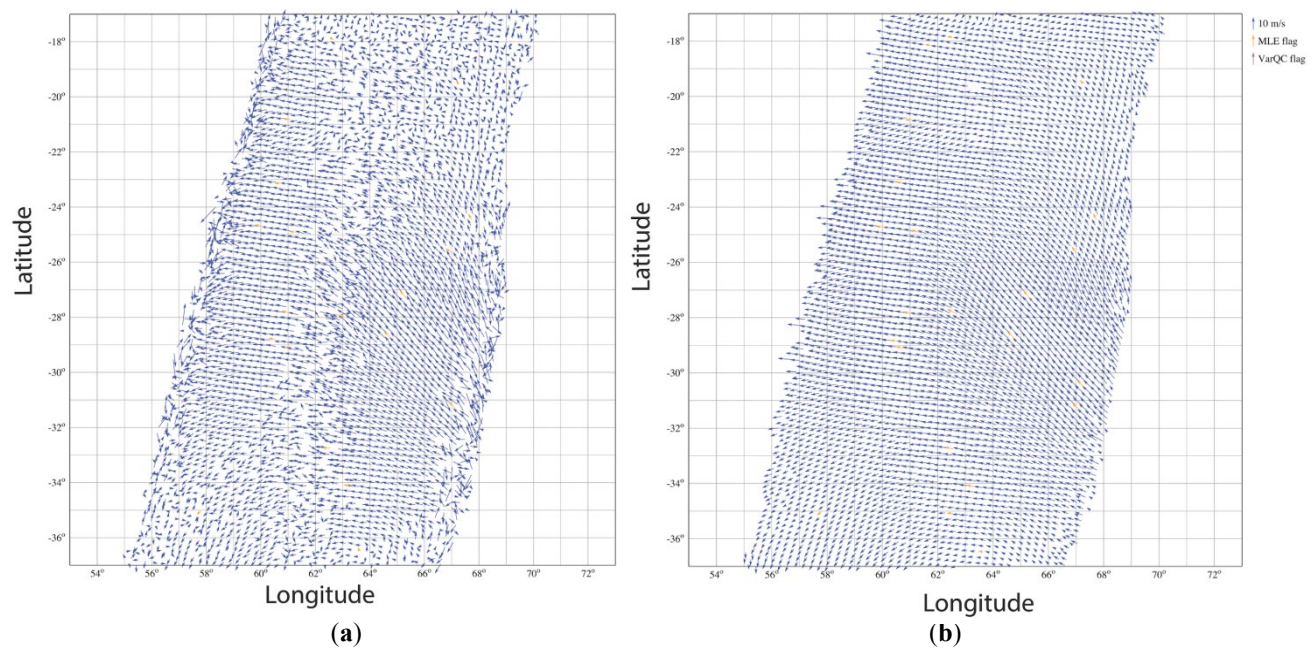


Figure 14 SCAT retrieved wind field. (a) 1st rank solution; (b) 2DVAR result. The orange flags are artificial QC points and may be ignored.

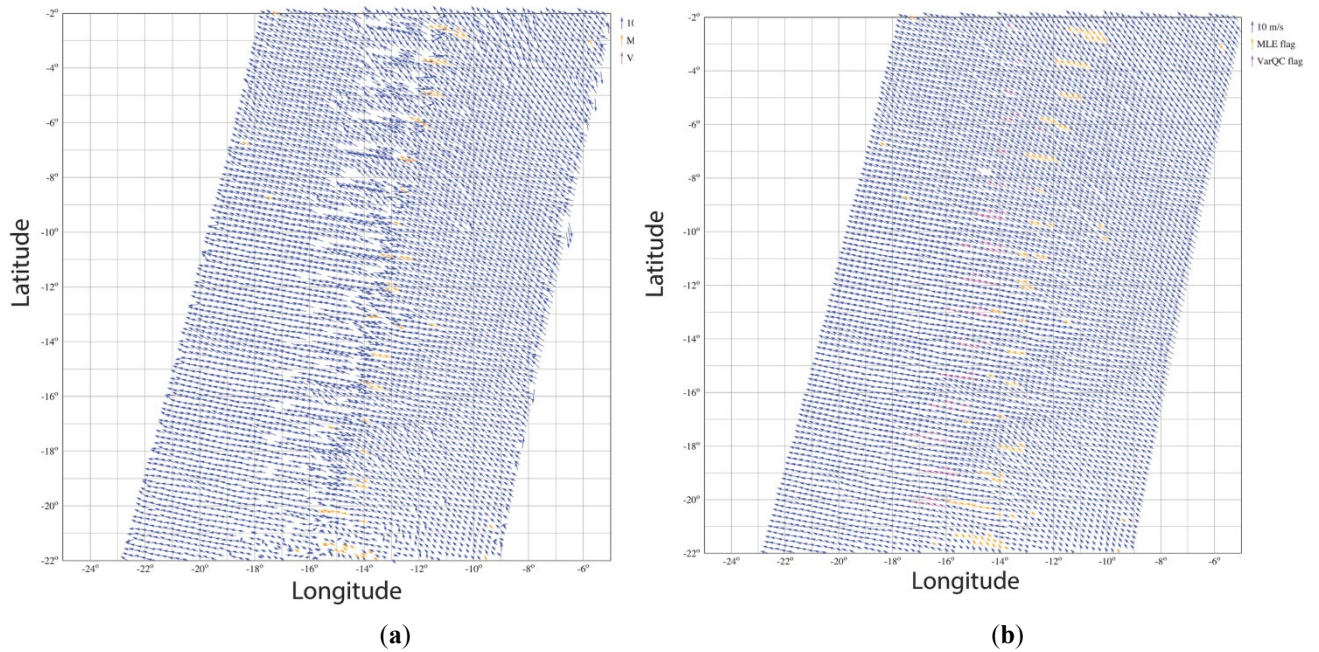


Figure 15 WindRad retrieved wind field. (a) 1st rank solution; (b) 2DVAR result. The orange flags are artificial QC points and may be ignored.

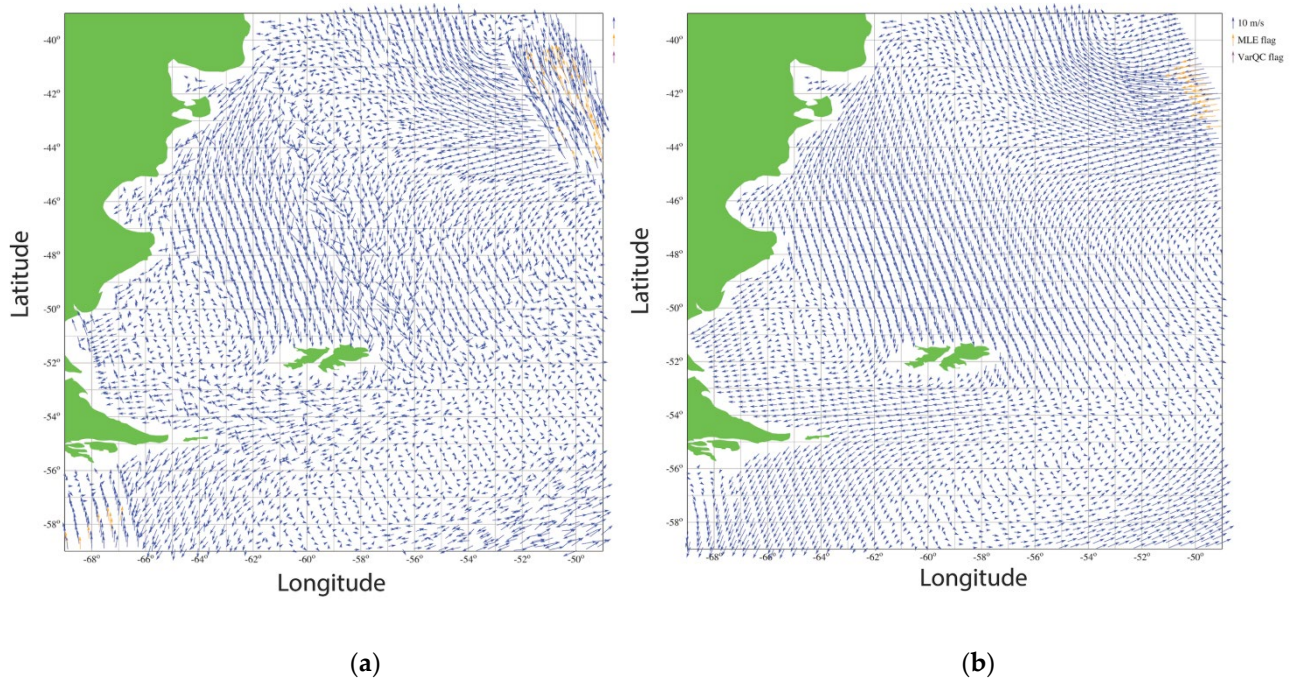


Figure 16 SeaWinds retrieved wind field. (a) 1st rank solution; (b) 2DVAR result. The orange flags are artificial QC points and may be ignored.

4.2 Wind retrieval performance evaluation

4.2.1 Assessments with the input wind field

Four orbits of data on 2011-12-17 have been generated to be used for the wind retrieval simulation. The contoured histograms in Figure 17 and Figure 18 provide statistics of the wind speed, clock-wise wind direction with respect to a wind blowing from the North, and wind vector components u (eastward) and v (northward) versus the variable “true” input wind field for SCAT and WindRad. ECMWF winds on 17 Dec. 2011 were taken as truth. We note that opposing wind solutions will have opposite u and v signs and similar amplitude and therefore such common ambiguity appears as a cross pattern in the u and v histograms. This ambiguity is directly related to the main double harmonic GMF dependency [18].

For SCAT (Figure 17 (a)), the 1st rank solutions of all WVCs across the swath are included. It shows rather poor statistics when compared with the input wind field. However, by simply excluding the WVCs located in the outer swath, the 1st rank solution quality improves substantially (Figure 17 (b)). The spread in the wind speeds is reduced and some derived false wind directions, which are shown as parallel and perpendicular lobes to the true value in the plots, are removed. When the nadir-swath WVCs are also excluded (Figure 17 (c)), then the wind speed collocation statistics stay almost unchanged as compared to Figure 17 b, while most of the false wind directions perpendicular to the true value are removed. This means that the outer swath contains the most ambiguous wind vector results, while the nadir swath ambiguities cause mainly wind direction errors.

Figure 18 (a) shows the 1st rank wind retrieval for WindRad with all WVCs and it shows much better statistics as compared to SCAT (Figure 17 (a)), due to twice the number of views in each WVC. Excluding outer WVCs (Figure 18 (b)) has less effect on the wind retrieval quality for WindRad than for SCAT. The retrieved wind speed shows a bit better statistic, but wind direction statistics stay almost unchanged, which means that the outer WVCs do not strongly increase the wind direction ambiguity. On the other hand, when we only exclude nadir WVCs (Figure 18c), the wind direction retrieval is improved. The average wind speed bias is 0.42 m/s and the standard deviation of wind direction is 32.21° (Figure 18 (c)), while they are 0.51 m/s and 41.30° for

Figure 18 (b), respectively. The last experiment shown for WindRad is to exclude both outer and nadir WVCs (Figure 18 (d)) with averaged wind speed bias of 0.44 m/s and standard deviation of wind direction of 35.61° . The largest performance improvement of WindRad occurs when excluding nadir WVCs. The outer swath mainly influences the wind speed retrieval skill, while the nadir swath provides wind direction ambiguity.

SeaWinds's outer swath contains only two views (fore-VV and aft-VV), and in order to process outer swath winds, each of these two views are split into two views based on their azimuth angle (four views in total in the end). Even though there are four views at the outer swath, the limited azimuth diversity leads to more ambiguous wind retrieval results (Figure 19). The wind retrieval quality of SeaWinds is the poorest one among these three instruments.

The averaged wind retrieval statistics against the input wind field are dominated by ambiguity and non-linearity. In practice these issues are successfully dealt with in the ambiguity removal step, using prior background information. In next section we determine Figures of Merit (FoM) to compare scatterometer performances with and without such prior information.

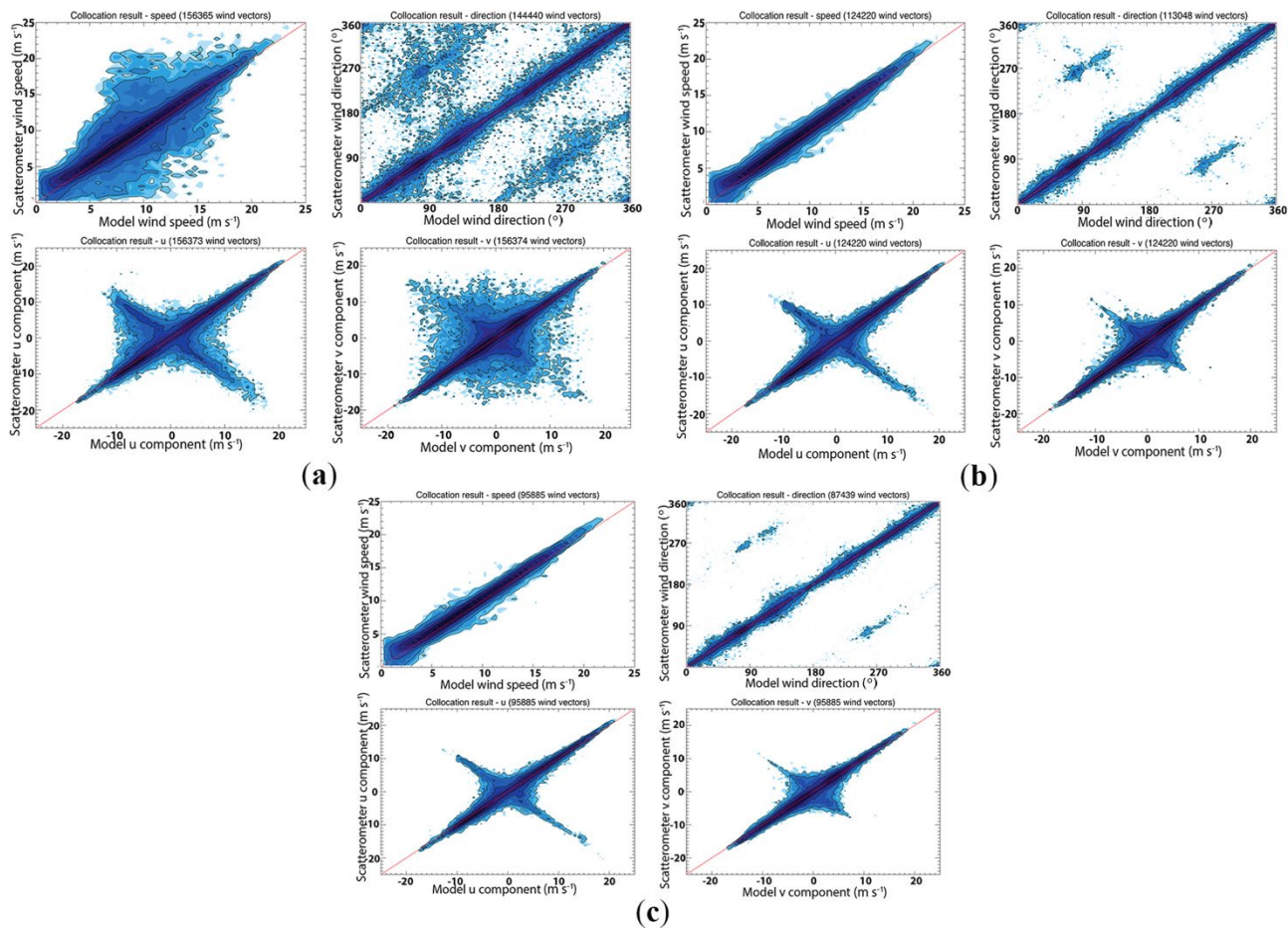


Figure 17 Contoured histograms of SCAT retrieved 1st rank wind solution versus input wind field for 4 orbits. (a) all WVCs within the swath; (b) excluding the WVCs in the outer swath, WVC numbers 8 to 42 are included; (c) excluding the WVCs in the outer swath and nadir swath, WVC numbers 8 to 17 and 26 to 42 are included. For (a) to (c), upper left: wind speed; upper right: wind direction; lower left: u component; lower right: v component. The contour lines are logarithmic.

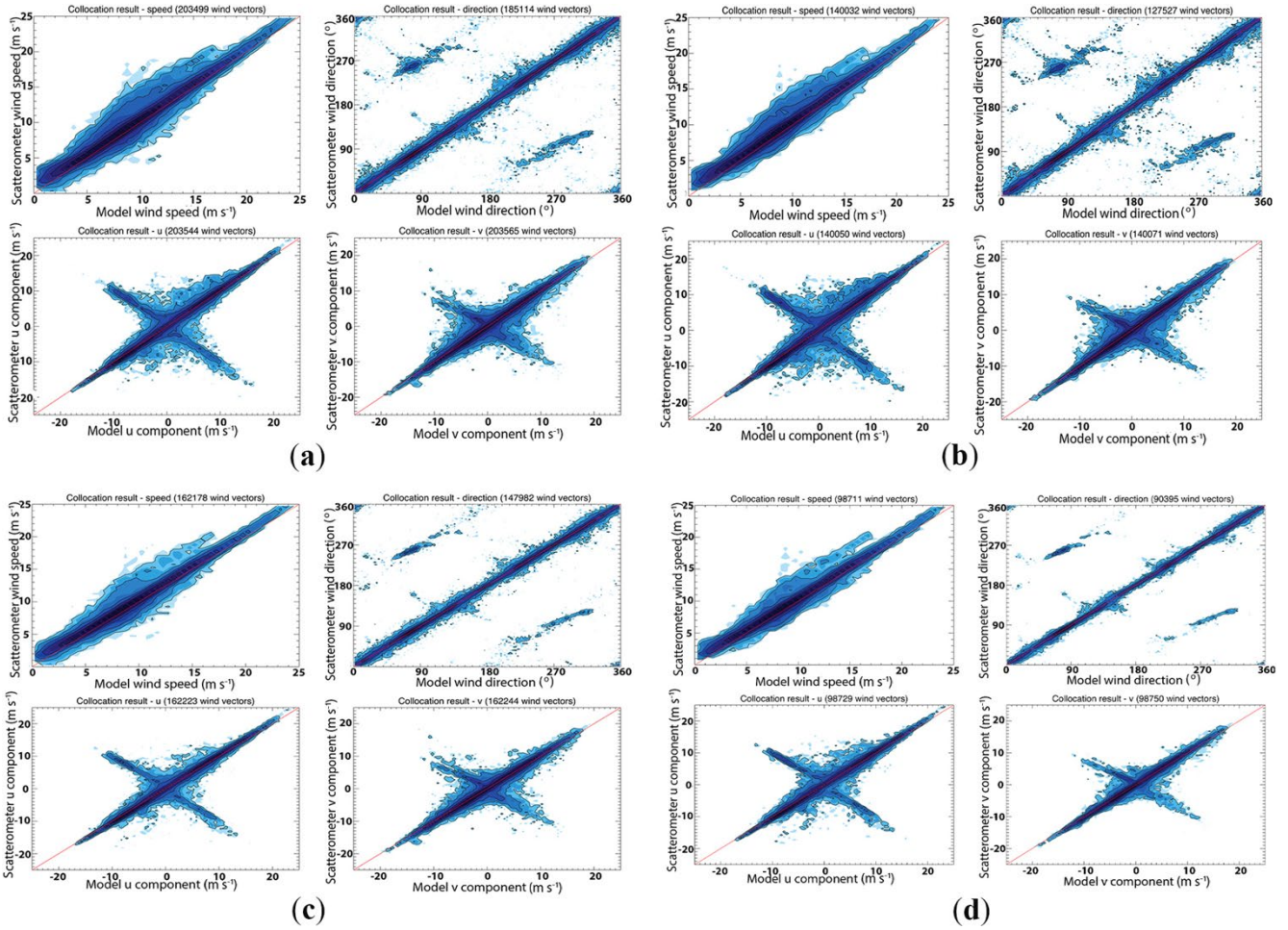


Figure 18 Contoured histograms of WindRad retrieved 1st rank wind solution versus input wind field for 4 orbits. (a) all WVCs within the swath; (b) excluding the WVCs in the outer swath, WVC numbers 20 to 60 are included; (c) excluding the WVCs in the nadir swath, WVC numbers 35 to 45 are included; (d) excluding the WVCs in the outer swath and nadir swath, WVC numbers 20 to 35 and 45 to 60 are included. The four figures in (a-d), upper left: wind speed; upper right: wind direction; lower left: u component; lower right: v component. The contour lines are logarithmic.

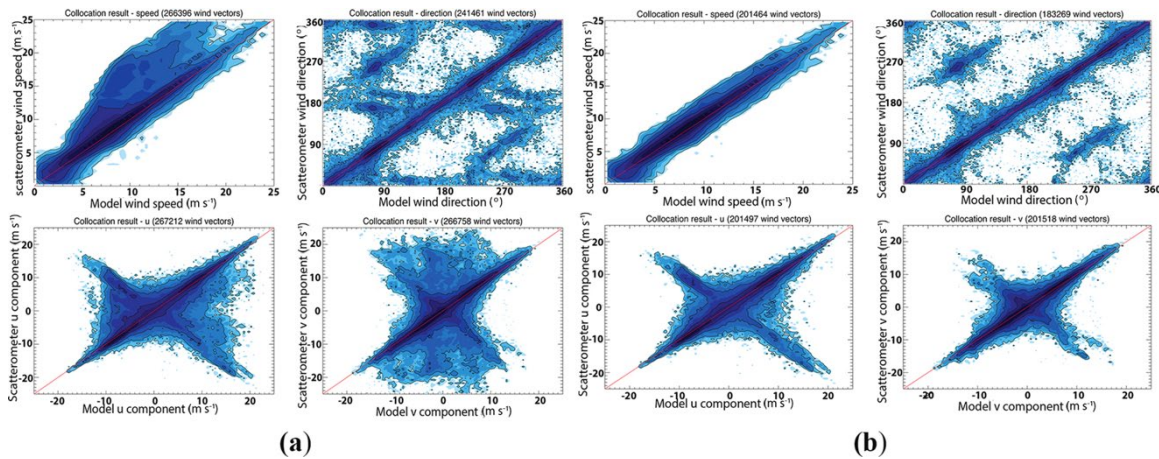


Figure 19 Contoured histograms of SeaWinds retrieved 1st rank wind solution versus input wind field for 4 orbits. (a) all WVCs within the swath; (b) excluding the WVCs in the outer swath, WVC numbers from 10 to 65 are included. From (a) to (b), upper left: wind speed; upper right: wind direction; lower left: u component; lower right: v component. The contour lines are logarithmic.

4.2.2 Figures of Merit

The 1st rank solutions contain ambiguities and because the input wind field is the ECMWF model wind, but without spatially correlated error, it leads to a nearly perfect 2DVAR result, which is unrealistic. As compared to true winds, ECMWF winds are rather smooth and the 2DVAR NWP input errors that we simulate are too simplistic (spatially uncorrelated and Gaussian). In order to further evaluate the wind retrieval performance, the ambiguity of the solutions may be statistically evaluated in the context of generally available background (NWP) information. Figures of Merit (FoM) are a set of parameters to evaluate the wind retrieval quality of different scatterometer concepts, taking into account imprecise, ambiguous and biased wind solutions. Three FoM, which are normalized wind Vector RMS error (VRMS), Ambiguity Susceptibility (AMBI) and systematic error (BIAS), are introduced here based on [19]. A brief description is given first.

The VRMS FoM is defined to quantify the ability of the scatterometer wind retrieval to handle ambiguous solutions with the aid of a priori NWP model information, such as in 2DVAR, but without actually simulating realistic spatially correlated errors. The input wind field to our simulation is considered as true winds (denoted with \vec{v}_t). VRMS quantifies the total simulated wind retrieval error with respect to \vec{v}_t . It is,

however, calculated by down-weighting ambiguous wind vector solutions that are very distant from \vec{v}_t , since in practice it is easiest for 2DVAR and other applications to discard such solutions. The down-weighting involves the common prior knowledge in these applications, which is the general NWP background wind component uncertainty, denoted σ_{NWP} and assumed equal for u and v. The ambiguous retrieved wind vector distribution, expressed in the wind probability $P_{obs}(\vec{v}|\vec{v}_t)$, is multiplied by a Gaussian probability distribution $P_{NWP}(\vec{v} - \vec{v}_t)$ centered at the input wind field and with a variance $\sigma_{NWP}^2 \sim 5 \text{ m}^2/\text{s}^2$ in both wind components. The VRMS FoM is subsequently obtained by normalizing this expression by the prior NWP VRMS error:

$$FoM_{VRMS} = \frac{RMS_{obs}}{RMS_{NWP}} \quad (2)$$

where $RMS_{obs} = \left(\sqrt{\int |\vec{v} - \vec{v}_t|^2 P_{obs}(\vec{v}|\vec{v}_t) \times P_{NWP}(\vec{v} - \vec{v}_t) d^2v} \right)$ and $RMS_{NWP} = \left(\sqrt{\int |\vec{v} - \vec{v}_t|^2 P_{NWP}(\vec{v} - \vec{v}_t) d^2v} \right) = \sqrt{2}\sigma_{NWP}$. VRMS quantifies the wind solution's relative RMS about the true wind with respect to the general prior background uncertainty. If its value is 1, then the wind retrieval failed to provide new and useful information in the wind field, i.e., corresponding to $P_{obs}(\vec{v}|\vec{v}_t) = \text{constant}$.

On the other hand, AMBI is defined to quantify the ability of the scatterometer and its processing to handle ambiguous solutions without a priori NWP model information. It is a ratio of the wind solution output falling outside the general prior wind field constraint, relative to the output falling inside the prior wind field constraint. The lower the ratio, the better (3), where $P_{NWP,max}$ is the maximum probability of $P_{NWP}(\vec{v} - \vec{v}_t)$.

$$FoM_{AMBI} = \frac{\int P_{obs}(\vec{v}|\vec{v}_t) \times (P_{NWP,max} - P_{NWP}(\vec{v} - \vec{v}_t)) d^2v}{\int P_{obs}(\vec{v}|\vec{v}_t) \times P_{NWP}(\vec{v} - \vec{v}_t) d^2v} \quad (3)$$

BIAS quantifies the systematic vector wind bias, again in the context of the background prior, which is the shift of the average location of the output wind solution away from the location of the prior wind caused by skewness in the output wind solutions (4).

$$FoM_{BIAS} = \int (\vec{v} - \vec{v}_t) \cdot P_{obs}(\vec{v}|\vec{v}_t) \times P_{NWP}(\vec{v} - \vec{v}_t) d^2v \quad (4)$$

The wind retrieval is a non-linear problem and the output wind error depends on the true wind vector (wind speed and direction distribution). In order to minimize this dependence, the calculated FoMs are averaged over a climatology of wind inputs with uniformly distributed directions and wind speeds (3 m/s to 16 m/s) following a Weibull distribution with a maximum around 8 m/s [20]. The input wind speeds are from 3 to 16 m/s with steps of 1 m/s, and the input wind directions are from 0 to 360 degrees with steps of 10 degrees. Each wind speed and wind direction combination contains the equivalent number of WVCs from the same orbit.

Figure 20 gives the three FoM comparisons of SCAT, WindRad and SeaWinds as a function of the WVC positions in the swath. Overall, the wind retrieval performance of the rotating fan-beam instruments is better than the pencil-beam instrument, while the outer and nadir swaths of the three instrument types yield a poorer performance than the sweet swaths. The outer swath of SeaWinds only has two independent views, which result in very ambiguous winds and the worst simulated wind retrieval quality. The wind retrieval quality across the swath strongly depends on the location of the WVC; it degrades substantially in the outer and nadir swaths as expected. The outer swath has worse quality than the nadir swath for both SCAT and SeaWinds, whereas these two regions are showing comparable wind retrieval quality for WindRad. Although the number of views in the sweet swath for WindRad is twice the number for SCAT (Figure 8), the wind retrieval quality is not improved as may be anticipated, but shows very similar quality to SCAT. The elevated values for AMBI and BIAS indicate that, despite the high number of views, the wind retrieval tends to be not well determined and slightly non-linear. At the same time, the quality in the outer swath of WindRad shows very pronounced improvement with respect to SCAT, due to the increased number of available views.

Figure 21 illustrates the VRMS as a function of wind direction and WVC location at 9 m/s wind speed. The wind retrieval performance across the swath for all wind directions gives the same pattern as described above with some modulations at different wind direction. There is one different feature occurring for WindRad. The VRMS at nadir swath shows higher values than in the outer swath, which is opposite to SCAT and SeaWinds. AMBI and BIAS (not shown here) have similar patterns as VRMS.

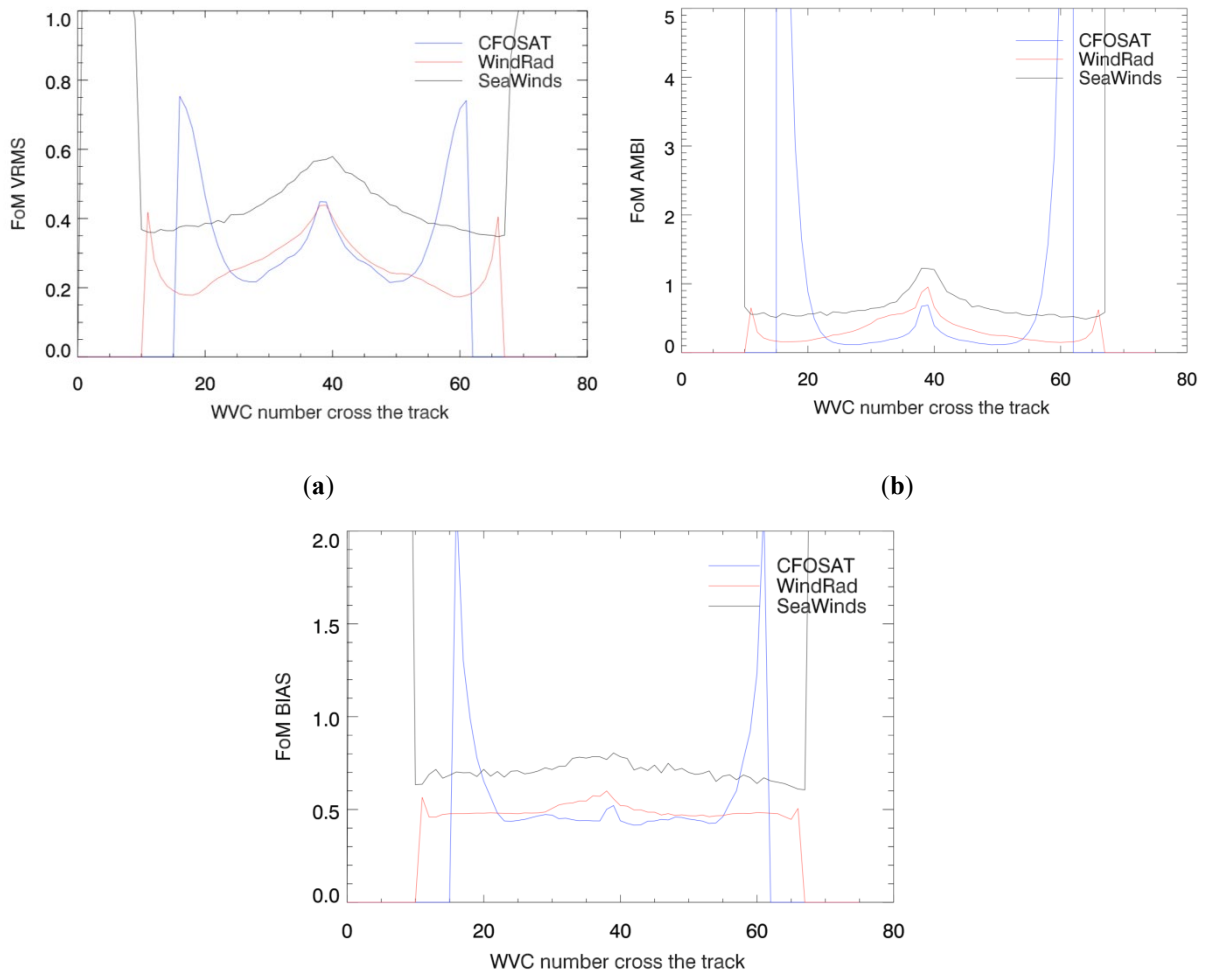


Figure 20: FoM results of SCAT, WindRad. (a) VRMS comparison; (b) AMBI comparison; (c) BIAS comparison.

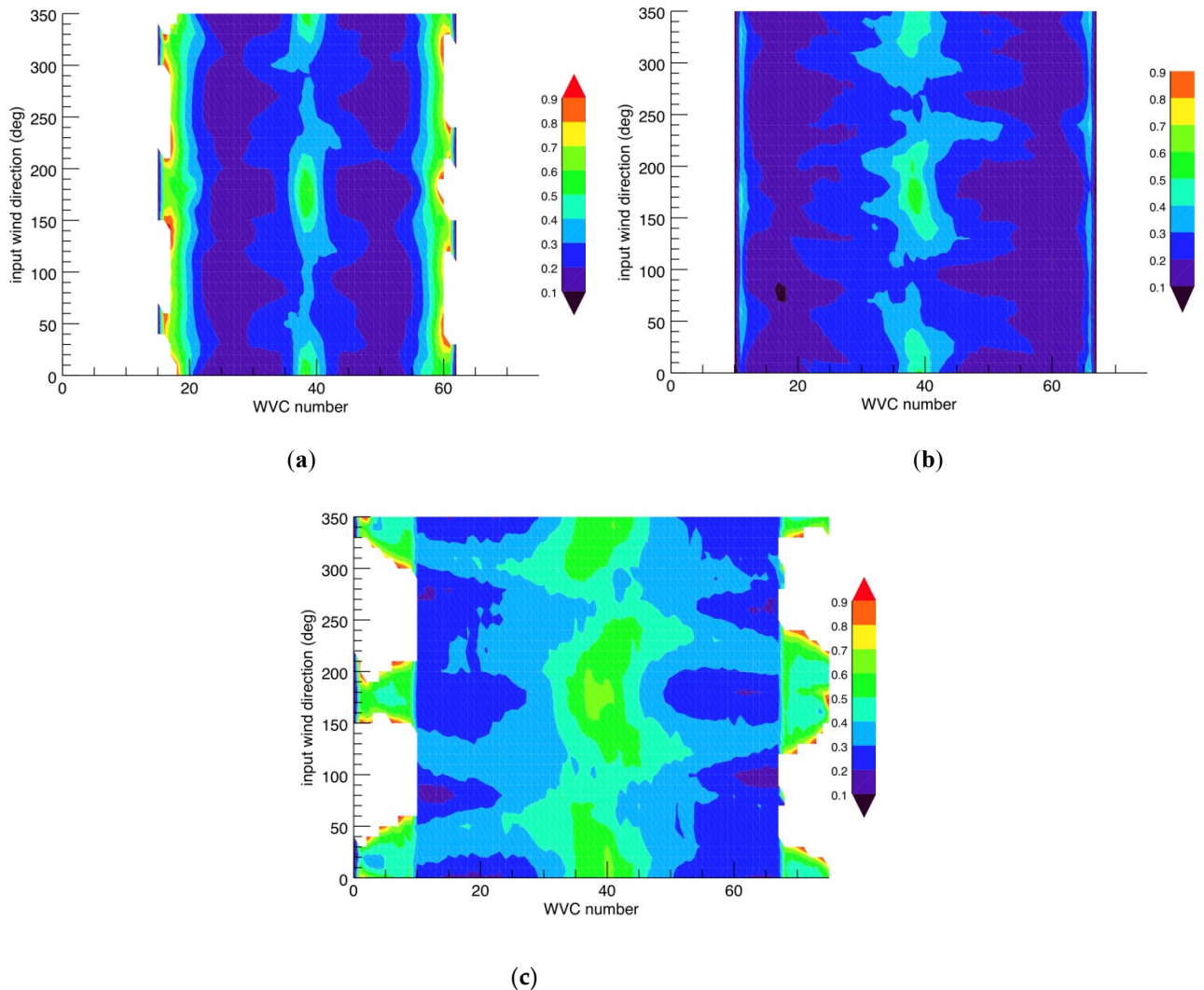


Figure 21: FoM VRMS map as a function of cross-track location and wind direction (wind speed is 9 m/s). (a) SCAT; (b) WindRad; (c) SeaWinds.

4.2.3 Wind direction bias

Wind direction bias between the wind retrieval result (2DVAR result) and the ECMWF model wind has been evaluated as a function of WVC and relative wind direction, using 15 orbits. The relative wind direction means the retrieved wind direction relative to the satellite motion direction. In this evaluation, we are able to see the wind direction bias with respect to the true direction at all the WVCs (Figure 22). No matter the biases are negative or positive, both signs indicate that the wind directions have a tendency to be closer to the satellite motion direction and if the wind direction

bias is averaged over all the relative wind directions, a small value of the bias remains.

SeaWinds gives stronger bias both on the outer swath and nadir swath (Figure 22 (b)), while the nadir swath of SCAT gives weaker bias comparing to the outer swath due to the increased number of views (Figure 22 (a)). For WindRad, when the retrieved wind direction is close to satellite motion direction (relative wind direction is 0), it shows rather strong negative and positive bias, but the non-biased area for WindRad is larger than it is in SCAT and SeaWinds. This phenomena can also be observed with real data from SCATSAT [21]. This retrieved wind direction preference might be caused by the retrieval method.

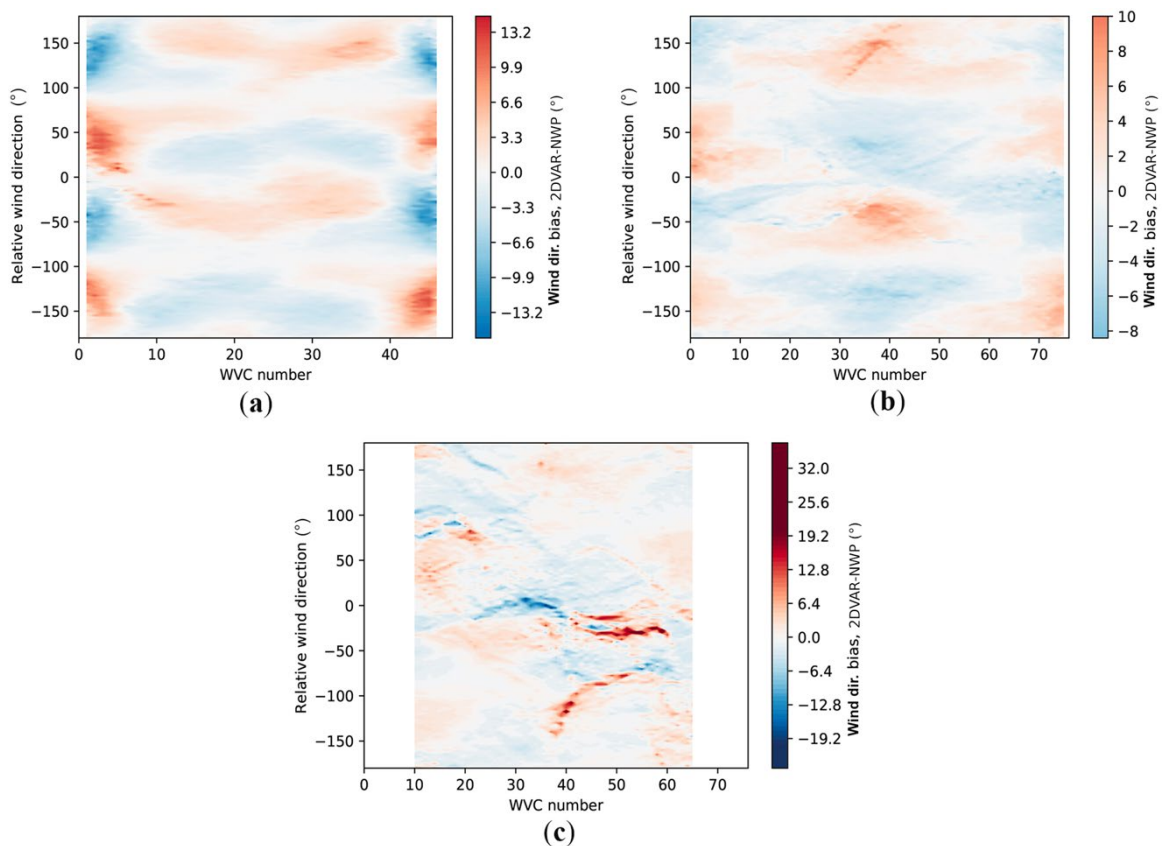


Figure 22 Wind direction bias between wind retrieval result and true wind as a function of WVC number and the relative wind direction (y-axis, the retrieved wind direction relative to the satellite motion direction; color scale is consistent for easy comparison, all the values outside [-20, 20] are marked as dark blue and dark red). (a) SCAT; (b) SeaWinds; (c) WindRad.

4.3 Wind direction skill optimization

One of the assumptions in the wind retrieval (see 4.1) is that the prior probability $P(\sigma^{\circ}_s)$ is constant. However, it is not the case in reality. In order to obtain accurate and realistic wind direction distribution after inversion, some attempts were made to account for a non-constant prior. For ERS, it was shown that it is desired that equal portions of the σ° triplets are thrown onto equal wind direction intervals, which implies that the favored GMF solution surface (i.e., cone surface) in measurement space is circular rather than elliptic [16]. A space transform was applied to achieve this goal by visualizing the GMF cone in a 3-D measurement space and scaling it into a circular cone, which is obtained in z-space ($z_i = (\sigma^{\circ}_i)^{0.625}$), and wind retrieval in z space shows improvement as compared to a space with Kp normalization [16]. But this method cannot be applied on RFSCAT, since the RFSCAT measurement system is far more than three dimensions and the transformation cannot be derived through the visualization in a 3-D measurement space. A more generic method has been proposed and tested on ERS and Seawinds named as Beam Weighting [22].

4.3.1 Beam weighting method

This more generic beam weighting method determines numerically the best space transformation to achieve constant $P(\sigma^{\circ}_s)$ instead of visualizing GMF solution surface [22]. The probability of a given infinitesimal set of points is the same in measurement space and in the wind domain, so the probability density $p(\sigma^{\circ}_s) = p(\mathbf{v}_s) \|\partial \mathbf{v}_s / \partial \sigma^{\circ}_s\|$. $p(\mathbf{v}_s)$ can be assumed as uniform for small variations of \mathbf{v}_s , while σ°_s and wind speed are quasi linear. Therefore, the dependency of σ°_s on wind direction mainly determines the modulation of $p(\sigma^{\circ}_s)$, i.e., $p(\sigma^{\circ}_s)$ can be modulated by the total wind direction sensitivity and constant total wind direction sensitivity means constant $p(\sigma^{\circ}_s)$. Now the optimization is transferred from achieving constant $p(\sigma^{\circ}_s)$ to achieving constant total wind direction sensitivity [22]:

$$\left\| \frac{\partial \sigma^{\circ}}{\partial \varphi} \right\| = \sum_{i=1}^N \left(\frac{\partial \sigma^{\circ}_i}{\partial \varphi} \right)^2 = \text{constant} \quad (5)$$

N is the number of beams (views). Normally this constant cannot be fulfilled, then a transformation is needed for the σ° , i.e., $\sigma^{\circ'} = a \cdot \sigma^{\circ}$, to make

$$\left\| \frac{\partial \sigma^{\circ}}{\partial \varphi} \right\| \approx \text{constant} \quad (6)$$

[22] tested this method on ERS and verified it with z-space transform, which shows beam weighting is as effective as z-space. Figure 22 shows where Beam Weighting plugs in. ERS WVCs all have three views with peaks and troughs phased differently. They do have rather consistent wind sensitivity at the same wind speed. However, the number and geometry of views for RFSCAT changes from one WVC to another, so the wind sensitivity also varies for each WVC. Some adaptations have been applied which are described as follows.

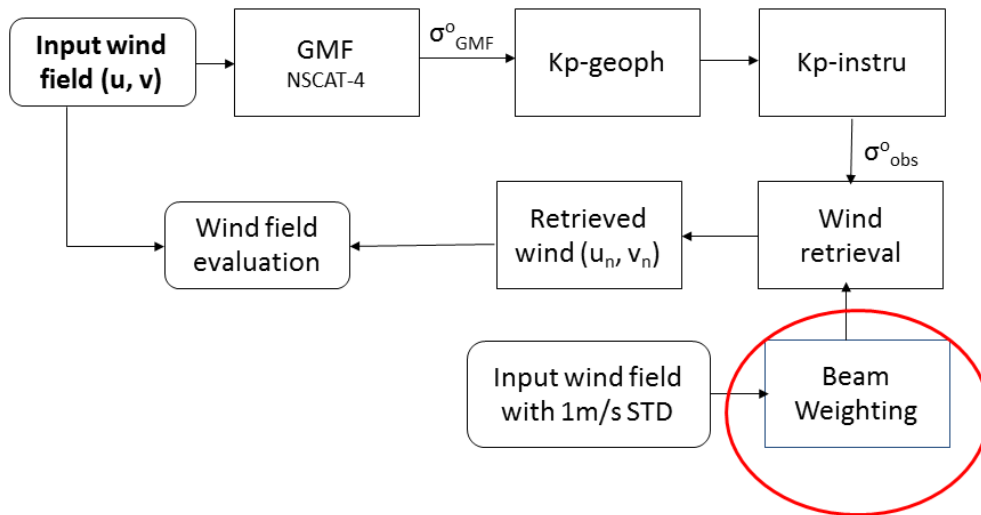


Figure 23 Beam Weighting method plug in.

A. Fourier series fitting

The computed wind direction sensitivity of SCAT is not smooth (not totally harmonic) due to the systematic error when the neighboring σ° are mutually subtracted during the calculation of the sensitivity, which introduces extra non-uniformity (noise) to the total sensitivity. Thus, Fourier series is applied to fit each sensitivity curve in order to remove the non-harmonic noise (Figure 10c) The mean total wind direction sensitivity:

Mean = $\frac{1}{M} \sum_{j=1}^M \sum_{i=1}^N \left(\frac{\partial \sigma_i^{\circ}}{\partial \varphi} |_{\varphi_j} \right)^2$. M is the number of wind direction intervals, here this

is 360.

B. Cost function

Our goal is to weight the sensitivities of various views in order to make the total wind direction sensitivity as flat as possible and as close to the mean as possible. A cost function is needed for this purpose:

$$J = \frac{1}{M} \sum_{j=1}^M \left[\sum_{i=1}^N \left(a_i \cdot \left. \frac{\partial \sigma_i}{\partial \varphi} \right|_{\varphi_j} \right)^2 - Mean \right]^2 \quad (7)$$

where J is the cost function and a_i is the beam weighting coefficient [22]. This cost function attempts to minimize the distance between the total wind direction sensitivity and the mean sensitivity. It is able to reduce the total distance between the mean sensitivity and the total sensitivity, but the gradient of the total sensitivity also needs to be minimized. In order to achieve this aspect, a second term is added to (7):

$$J_2 = \sum_{j=1}^M \sum_{i=1}^N \left\{ a_i^2 \cdot \left[\left(\frac{\partial \sigma_i}{\partial \varphi_{i,j+1}} \right)^2 - \left(\frac{\partial \sigma_i}{\partial \varphi_{i,j}} \right)^2 \right] \right\}^2 \quad (8)$$

J_2 minimizes the total gradient of the total sensitivity. Initially, J_2 has the same weight as J , which is $J = A \cdot J_2$, and the new cost function is $J + A \cdot J_2$:

$$J_{new} = \frac{1}{M} \sum_{j=1}^M \left[\sum_{i=1}^N \left(a_i \cdot \left. \frac{\partial \sigma_i}{\partial \varphi} \right|_{\varphi_j} \right)^2 - Mean \right]^2 + A \cdot \sum_{j=1}^M \sum_{i=1}^N \left\{ a_i^2 \cdot \left[\left(\frac{\partial \sigma_i}{\partial \varphi_{i,j+1}} \right)^2 - \left(\frac{\partial \sigma_i}{\partial \varphi_{i,j}} \right)^2 \right] \right\}^2 \quad (9)$$

Figure 23 shows an example of the comparison between J and J_2 . Unfortunately, the result of modified cost function (Figure 23b) gives less gradient in total, but it introduces shaper non-harmonic features to the total wind direction sensitivity. So, the cost function (7) is chosen here. The BFGS (Broyden-Fletcher-Goldfarb-Shanno) algorithm is applied to minimize the cost function.

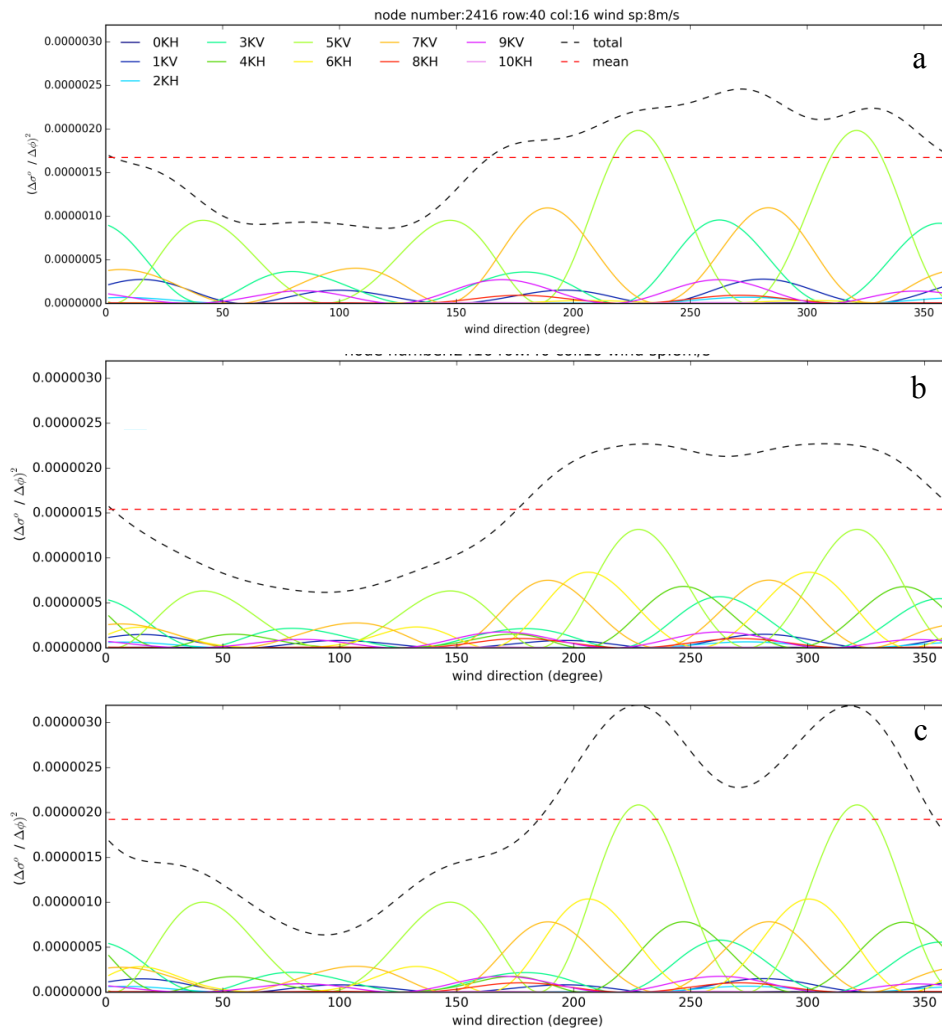


Figure 24 Cost function result comparison for WVC number 16 in sweet swath (a: $J_{new} = J + A \cdot J_2$, b: J , c: original without beam weighting).

4.3.2 Beam weighting various settings and comparison

Each WVC contains various number of views and every view has different instrument noise K_p . This is very different from the tested case of ERS [22], whose WVC contains three views with similar K_p . In the latter case, only moderate beam weights are needed and the variation in noise over the three views plays a minor role, facilitating the retrieval optimization. Similarly, for RFSCAT, if all the views had comparable K_p noise, then the beam weighting only needs to look for the coefficients which make the total wind sensitivity flat. However, the coefficients for the views with various K_p need to minimize the cost function (flatten the total wind direction sensitivity) without amplifying the noisy views with high K_p . So, the weights better

satisfy the condition that the views with high K_p are assigned a coefficient value less than 1 to avoid amplifying K_p noise in the wind retrieval, while the views with low K_p have a preference to be amplified in the beam weighting process. However, this condition is often not satisfied in reality because the differently phased peaks and troughs are often not fit to this condition. Another important factor is the multiple views. The number of views of SCAT is up to 18 in the sweet swath, which is much more than the three views of ERS. It leads to a more complex non-linearity effect to wind retrieval and beam weighting.

A. The beam weighting method with K_p taken into the cost function.

The various K_p is considered in the cost function:

$$J = \frac{1}{M} \sum_{j=1}^M \left[\sum_{i=1}^N \left(a_i \cdot \frac{\partial \sigma^\circ_i / K_{p_i}}{\partial \phi} \Big|_{\phi_j} \right)^2 - \text{Mean} \right]^2 \quad (10)$$

The WVCs from row number 403 from 2011-12-17 are chosen to illustrate the beam weighting method on SCAT. The cost function has a preference for the views which have solitary phased sensitivity peaks and troughs to compensate with proper coefficients and suppresses the other views. Since the coefficients have to be positive, some views are suppressed with coefficients almost zero, which views will thus no longer inform the wind retrieval. A soft limit constraint is applied on the coefficients: if the coefficient is less than one, then $\text{coefficient} = 1 - \text{sd} \times \text{gaussian_random_number}$, (sd: standard deviation, set to 0.5). In this way, the scaled total sensitivity may not be the flattest possible, but it keeps information from all views. The sensitivity of views with HH polarization is very low compared to the views with VV polarization, which means that the scaling systematically suppresses HH polarization views (Figure 24). To prevent this, the coefficients of the views with HH polarization are set to 1. Figure 25 shows an example with WVC 7 from row 403. The comparison of the total wind direction sensitivity before and after beam weighting shows that the beam weighting is able to effectively flatten the total sensitivity and it makes the prior assumption of constant $P(\sigma^\circ_s)$ become more realistic. To be noted is that the WVCs located at the side and

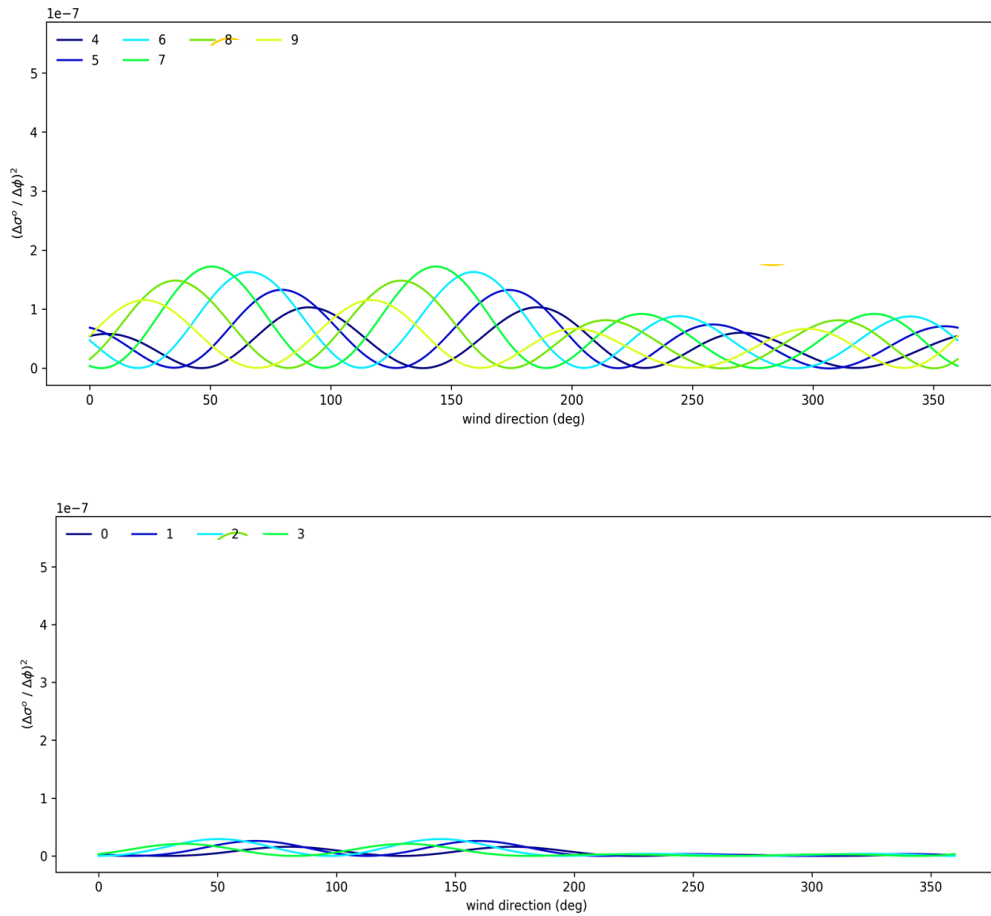


Figure 25 VV polarization sensitivity (upper) and HH polarization sensitivity (lower)

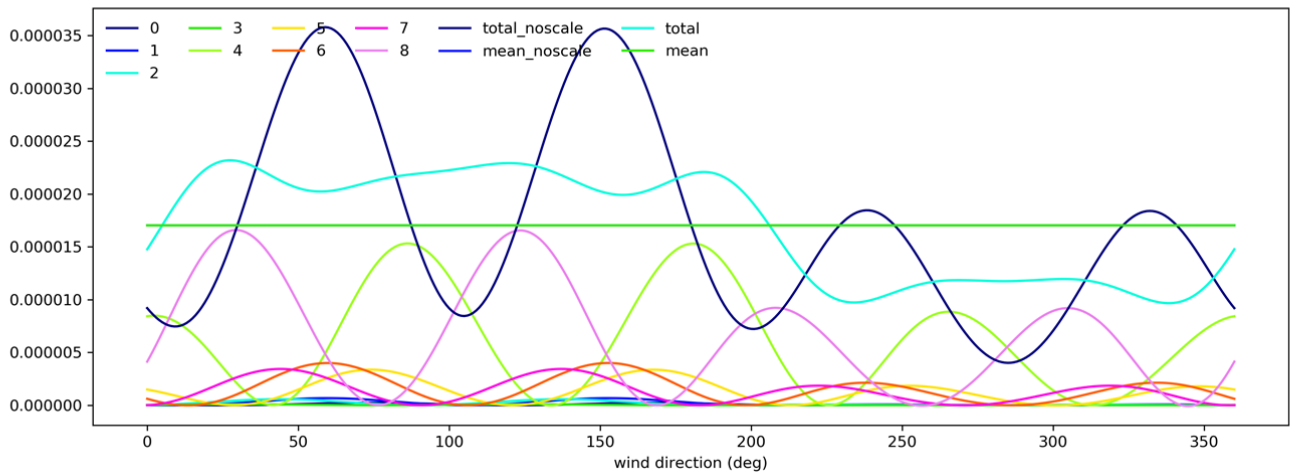


Figure 26 Wind direction sensitivity of WVC number 7 from row number 403, dark blue is the original total sensitivity, light blue is the scaled total sensitivity, the straight line is the mean sensitivity (original and scaled mean sensitivity are the same value, so they are overlapped), the colorful lines are the scaled views. View number 0 to 3 are HH polarization.

Table 4. FoM comparison with and without beam weighting (WVC 7, row 403)

view nr & polarization	0 HH	1 HH	2 HH	3 HH	4 VV	5 VV	6 VV	7 VV	8 VV	FoM		
Kp	0.31	0.20	0.21	0.41	0.32	0.11	0.10	0.11	0.21	VRMS	BIAS	AMBI
coefficient	1.0	1.0	1.0	1.0	3.72	0.53	0.503	0.55	2.28	0.315	0.432	0.433
no beam weighting										0.301	0.521	0.416

nadir of the swath are effectively scaled, due to their aligned peaks and troughs caused by the limited diversity of their azimuth angles. Table 4 evaluates the wind retrieval performance before and after beam weighting. It shows improvement in FoM_{BIAS} , but not the other FoMs. Similar FoMs results are shown on other WVCs as well, such as WVC 5 and WVC 13 (Figure 26, Figure 27, and Table 5, Table 6), but while for WVC 19, there is no improvement even though the scaled total sensitivity is flattened (Figure 28, Table 7).

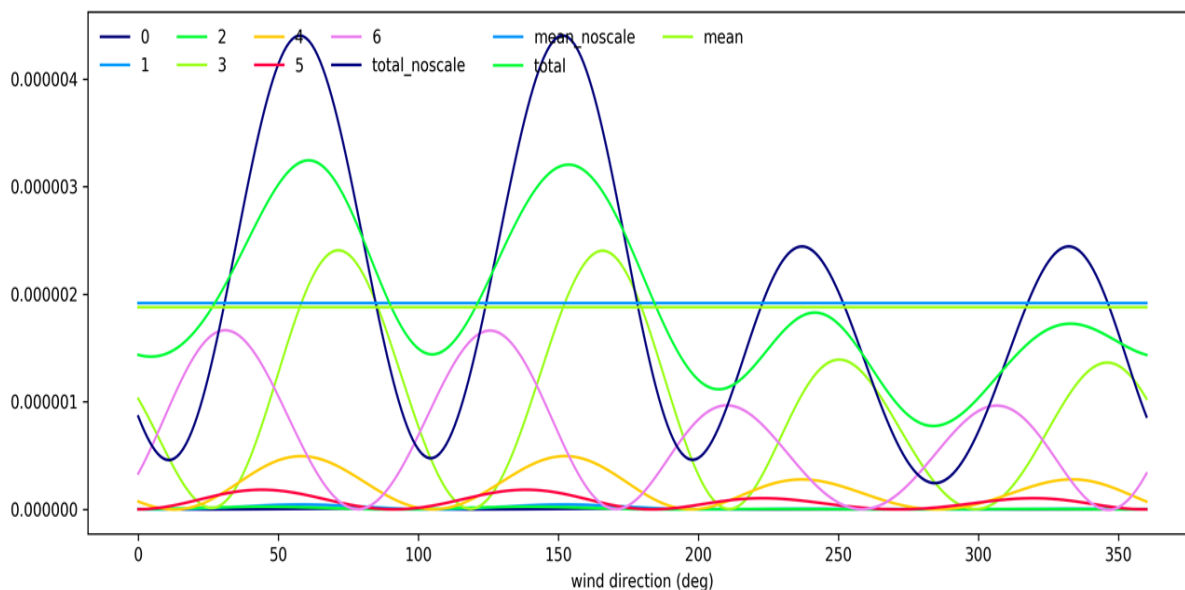


Figure 27 Wind direction sensitivity of WVC number 5 from row number 403 after beam weighting comparison with the total sensitivity before beam weighting (dark blue).

Table 5. FoM comparison with beam weighting and without beam weighting (WVC 5, row 403)

view nr & polarization	0 HH	1 HH	2 HH	3 VV	4 VV	5 VV	6 VV	FoM		
	Kp	1.29	0.55	0.71	0.38	0.25	0.36	0.80	VRMS	BIAS
coefficient	1	1	1	1.520	0.434	0.416	3.359	0.580	1.183	1.889
no beam weighting								0.564	1.278	1.853

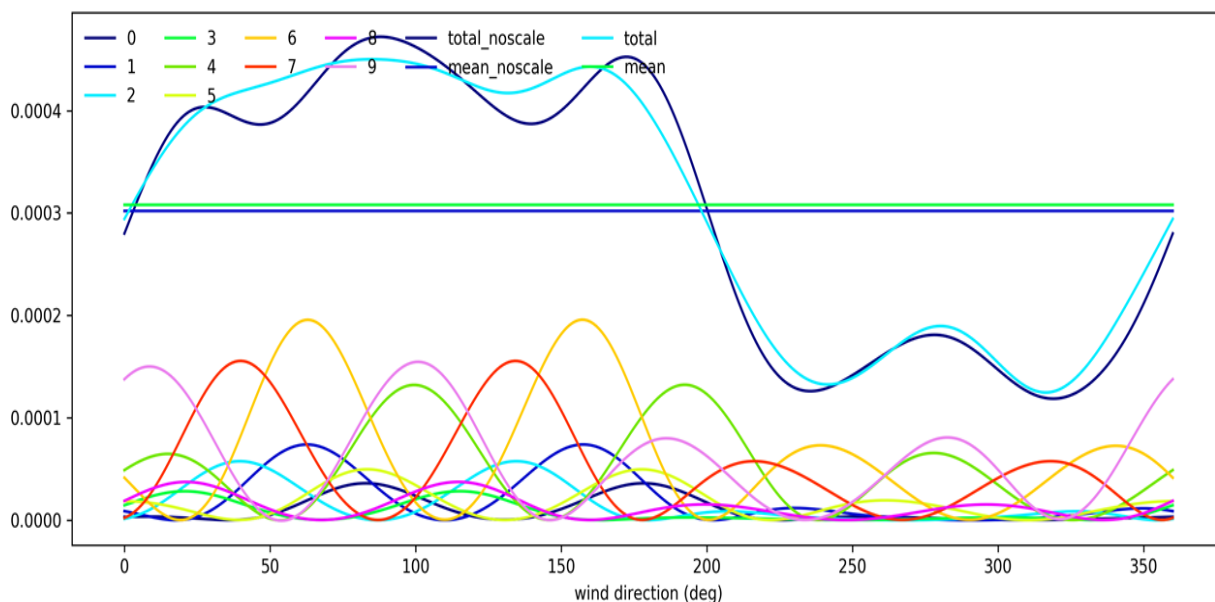


Figure 28 Wind direction sensitivity of WVC number 13 from row number 403 after beam weighting comparison with the total sensitivity before beam weighting (dark blue)

Table 6. FoM comparison with beam weighting and without beam weighting (WVC 13, row 403).

view nr & polarization	0 HH	1 HH	2 HH	3 VV	4 VV	5 VV	6 VV	7 VV	8 VV	9 VV	FoM		
	Kp	0.073	0.085	0.084	0.070	0.048	0.051	0.082	0.087	0.054	0.047	VRMS	BIAS
coefficient	1.0	1.0	1.0	1.0	1.2	0.53	1.2	1.16	0.52	1.6	0.131	0.395	0.049
no beam weighting											0.127	0.399	0.048

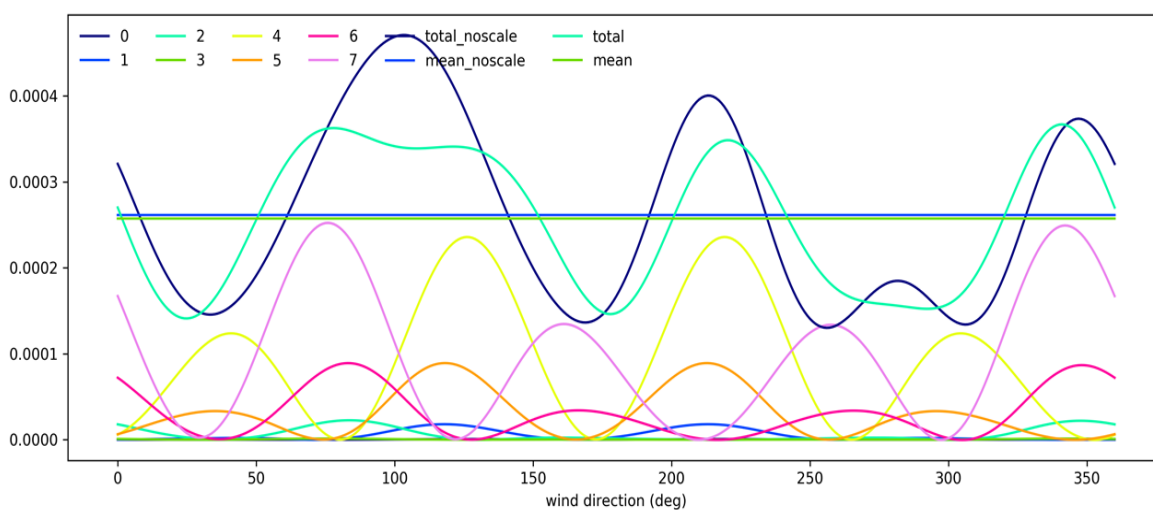


Figure 29 Wind direction sensitivity of WVC number 19 from row number 403 after beam weighting comparison with the total sensitivity before beam weighting (dark blue).

Table 7. FoM comparison with and without beam weighting (WVC 19, row 403).

view nr & polarization	0 HH	1 HH	2 HH	3 HH	4 VV	5 VV	6 VV	7 VV	FoM		
Kp	0.12	0.06	0.05	0.09	0.05	0.049	0.047	0.053	VRMS	BIAS	AMBI
coefficient	1.0	1.0	1.0	1.0	1.708	0.533	0.559	1.820	0.204	0.366	0.121
no beam weighting									0.192	0.364	0.110

B. The beam weighting method without taking Kp into the cost function.

In comparison with A., the cost function remains the same as in (7) in this section. WVC 7 from row 403 is used to apply beam weighting. Figure 29 shows that the total sensitivity after beam weighting is flattened comparing with before beam weighting and the mean total sensitivity keeps the same with and without beam weighting. All the FoMs evaluation (Table 8) shows that the beam weighting without Kp in the cost function is not able to improve the wind retrieval performance and also gives a worse performance in comparison with Table 4.

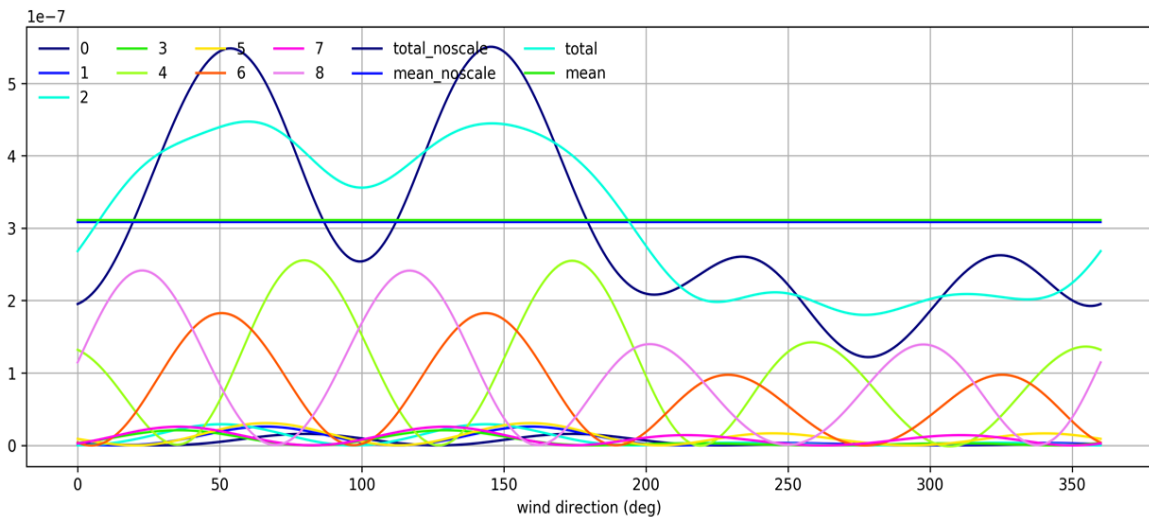


Figure 30 Wind direction sensitivity of WVC number 7 from row number 403 after beam weighting comparison with the total sensitivity before beam weighting (dark blue), Kp is not considered in the cost function.

Table 8. FoM comparison with beam weighting and without beam weighting (WVC 7, row 403, K_p is not considered in the cost function).

view nr & polarization	0 HH	1 HH	2 HH	3 HH	4 VV	5 VV	6 VV	7 VV	8 VV	FoM		
										VRMS	BIAS	AMBI
Kp	0.31	0.20	0.21	0.41	0.32	0.11	0.10	0.11	0.21	0.490	1.754	1.096
coefficient	1.0	1.0	1.0	1.0	1.39	0.43	1.03	0.42	1.45	0.301	0.521	0.416
no beam weighting												

C. The beam weighting method with constant K_p on all the views.

In this section, K_p is set to a constant number 0.1 in the simulation to all the views in order to rule out the impact of the various K_p on each view for beam weighting method. The result of WVC 11 from row 403 is shown here (Table 9, Figure 30). It is obvious that the scaled total sensitivity is more flatten than no scaled total sensitivity and the mean total sensitivity is the same with and without beam weighting, but the FoMs indicate that the wind retrieval with beam weighting does not improve the performance and very close to the result without beam weighting.

In summary, when K_p is not considered in the beam weighting, the FoMs show much worse result comparing without beam weighting, while when K_p is considered in the beam weighting, there is only slight improvement shown in FoM_{bias} . When we set the K_p the same value for all the views, the beam weighting FoMs keep very close to the results without beam weighting. The K_p instrument noise plays a dominant role in the wind retrieval optimization (beam weighting), where noisy views are often given more weight than views with good SNR. We believe that this follows from the rotating geometry and the consequent azimuth distribution at each WVC. It results indeed in reduced non-linearity in the sweet swath as anticipated, but unfortunately also in more noisy retrievals, i.e., increased RMS error and ambiguity. This makes the beam weighting method is not effective for the rotating fan-beam scatterometer because beam weighting also make the noise higher while make the sensitivity more constant.

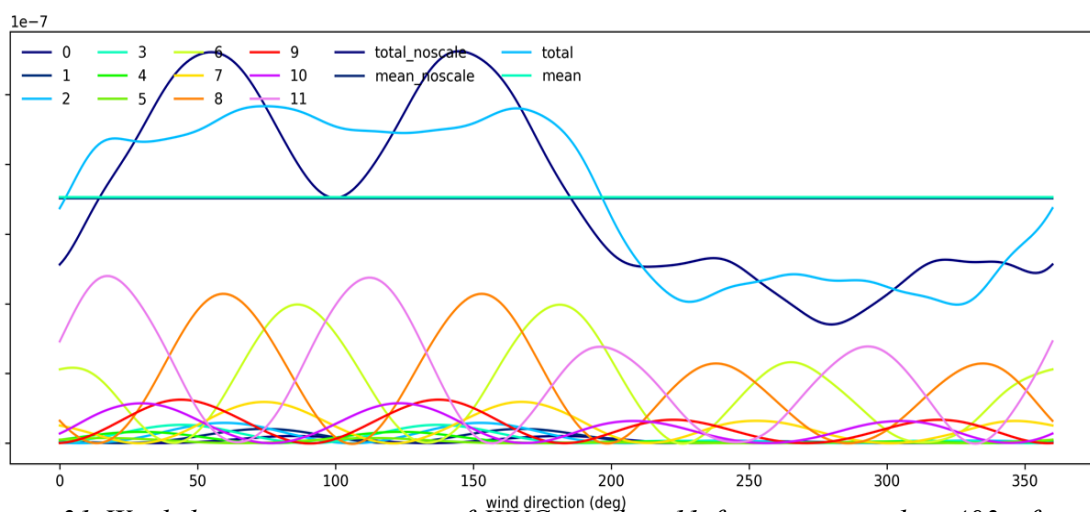


Figure 31 Wind direction sensitivity of WVC number 11 from row number 403 after beam weighting comparison with the total sensitivity before beam weighting (dark blue), all the views are with same Kp value 0.1.

Table 9 FoM comparison with beam weighting and without beam weighting, Kp = 0.1 (WVC 11, row 403).

view nr & polarization	0	1	2	3	4	5	6	7	8	9	10	11	FoM		
	HH	HH	HH	HH	HH	HH	VV	VV	VV	VV	VV	VV	VRMS	BIAS	AMBI
Kp	0.1	0.1	0.1	0.1	0.1	0.1	0.1	0.1	0.1	0.1	0.1	0.1	0.161	0.379	0.047
coefficient	1.0	1.0	1.0	1.0	1.0	1.0	1.33	0.63	1.11	0.62	0.65	1.55	0.161	0.379	0.047
no beam weighting	-	-	-	-	-	-	-	-	-	-	-	-	0.156	0.347	0.043

5. Conclusions

In summary, we have presented and assessed a generic simulation framework, which has been adapted to all existing rotating-beam scatterometer types (RFSCAT and rotating pencil-beam). A representative set of SCAT, WindRad and SeaWinds data are chosen to evaluate the wind retrieval performance of the rotating scatterometers using Ku-band. The wind retrieval quality strongly depends on the location of the WVCs across the swath, and the sweet swath shows the most favourable geometries for wind retrieval. Among the more unfavourable outer and nadir swath regions, SCAT and SeaWinds perform best in the nadir swath, while WindRad rather substantially improves the outer swath wind retrieval. On the other side, WindRad's nadir swath region with lower wind retrieval quality is larger than its outer swath region, while SCAT and SeaWinds have a relatively large outer swath region with degraded quality. The outer swath of SCAT implies both wind speed and wind direction retrieval problems, while for WindRad only wind speed retrieval is affected. Although rotating fan-beam scatterometers, particularly SCAT, much improve nadir performance with respect to SeaWinds. The nadir swath shows still significant wind direction ambiguity for both SCAT and WindRad.

The increased number of views in the nadir and sweet swath for WindRad does not lead to an improved wind retrieval, but it shows a saturation effect and stays relatively similar to SCAT. Since all GMF coefficients depend on incidence angle in a non-linear way, averaging may not always be accurate. One possible solution is to aggregate only slices with the same number, and it still needs to be tested. The retrieved wind direction has a tendency towards the satellite motion direction for both instruments, which is related to non-linear aspects of the retrieval procedure. The rain effect is not taken into consideration, so the rain disturbance in Ku-band and the advantage of the C-band on WindRad cannot be shown here.

To facilitate good quality collocations with the CFOSAT SWIM instrument, the design is clearly focused on an optimal performance close to nadir and employs small incidence angles, combined with a large incidence angle range. This facilitates the availability of additional views near nadir with enhanced azimuth and incidence angle diversity. On the other hand, WindRad's most useful complement is clearly its dual

frequency capability, providing many views in the outer swath, where excellent performance is obtained according to our simulations.

The developed simulation package allows us to further investigate the true resolution of the instruments before their launch and also to determine the non-overlap of the views in a WVC, which contributes to the geophysical noise. The WVC size is not the true spatial resolution and neither the true representation of the contributing views, which depend on the spatial response function of each sample, how these are aggregated into a view and which views contribute to the WVC [23], [24]. For rotating-beam scatterometers the sampling and hence wind retrieval characteristics vary potentially both by cross-track and along-track WVC, which may be further investigated. Such development may much help users interested in coastal winds.

Our simulation does not consider the rain effect. Ku-band ocean returns are affected by rain, and moderate and heavy rain will certainly degrade the wind retrieval. At KNMI, we use the wind retrieval MLE for rain screening of Ku-band systems, much aided by MSS 2DVAR. This successful methodology developed for SeaWinds will also be attempted for SCAT. On the other hand, C-band backscatter is much less sensitive to rain and included in WindRad. This advantage of WindRad should be further investigated, e.g., by using collocated measurements of Ku-band and C-band scatterometers in a combined wind retrieval.

Following successful application for ERS and ASCAT, the beam weighting method is tested on SCAT in order to suppress potential wind retrieval biases due to non-linearity (non-constant prior). The most important difference between SCAT and the tested case ERS is that there are much more views in one WVC and each view has a rather different instrument noise. The instrument noise has been taken into account and the FoMs show indeed BIAS has slightly improved as was our objective. However, both RMS error and ambiguity generally increase, probably due to increased weights of noisy views. In order to assess the influence of instrument noise, all the K_p 's are set to 0.1 for each view, and even if the scaled total wind direction sensitivity gives satisfied flatness, now all FoMs are slightly worse than without beam weighting method, including BIAS. In conclusion, the beam weighting method is not suitable to improve wind direction retrieval for the rotating fan-beam scatterometer due to the variation and domination of the K_p instrument noise in the WVCs.

Instead, the current non-linear MLE retrieval may be kept, but prior knowledge on its biases may be implemented. This will be subject of further research with real data.

The broad user community looks forward to an increased temporal sampling of the ocean surface with scatterometer winds, such as with both WindRad and SCAT, that will be useful contributions to the global ocean surface vector winds virtual constellation.



References

- [1] M. Portabella, “Wind Field Retrieval from Satellite Radar Systems,” 2002.
- [2] A. Stofflen, “Scatterometry,” Utrecht University, 1996.
- [3] Z. Li, A. Stoffelen, and A. Verhoef, “A Generalized Simulation Capability for Rotating Beam Scatterometers,” *Atmos. Meas. Tech.*, vol. 12, pp. 3573–3594, 2019.
- [4] J. Figa-Saldaña, J. J. W. Wilson, E. Attema, R. Gelsthorpe, M. R. Drinkwater, and A. Stoffelen, “The advanced scatterometer (ascat) on the meteorological operational (MetOp) platform: A follow on for european wind scatterometers,” *Can. J. Remote Sens.*, vol. 28, no. 3, pp. 404–412, 2002.
- [5] JPL, “QuikSCAT Science Data Product User’s Manual,” 2001.
- [6] C. C. Lin, B. Rommen, J. J. W. Wilson, F. Impagnatiello, and P. S. Park, “An analysis of a rotating, range-gated, fanbeam spaceborne scatterometer concept,” *IEEE Trans. Geosci. Remote Sens.*, vol. 35, no. 5, pp. 2114–2121, 2000.
- [7] C.-C. Lin, A. Stoffelen, J. De Kloe, V. Wismann, S. Bartha, and H.-R. Schulte, “Wind retrieval capability of rotating, range-gated, fanbeam spaceborne scatterometer,” in *Proc. SPIE Int. Symp. Remote Sens.*, 2002, pp. 268–285.
- [8] F. Dou, H. Yin, and S. Gu, “Simulation of wind performance in tropical cyclone for China’s future dual-frequency wind field radar,” in *Proc. of SPIE*, 2014, vol. 9264, pp. 92641G1-92641G7.
- [9] F. R. Hoots and R. L. Roehrich, “Spacetrack Report No. 3-Models for Propagation of NORAD Elements Sets,” 1980.
- [10] F. J. Wentz and D. K. Smith, “A model function for the ocean-normalized radar cross section at 14 GHz derived from NSCAT observations,” *J. Geophys. Res.*, vol. 104514, no. 15, pp. 499–11, 1999.
- [11] A. Verhoef, M. Portabella, A. Stoffelen, and H. Hersbach, “CMOD5. n-the CMOD5 GMF for neutral winds,” 2008.
- [12] R. S. Dunbar, S. V. Hsiao, Y. Kim, K. S. Pak, B. H. Weiss, and A. Zhang, “Science Algorithm Specification,” *Jet Propuls.*, 2001.
- [13] Z. Li, A. Verhoef, and A. Stofflen, “CWDP L1B simulator and L2A processor Specification and User Manual,” de Bilt, the Netherlands, 2017.
- [14] C. Y. Chi and F. K. Li, “A comparative study of several wind estimation algorithms for spaceborne scatterometers,” *IEEE Trans. Geosci. Remote Sens.*, vol. 26, no. 2, pp. 115–121, 1988.
- [15] “Probabilities and statistics for backscatter estimates obtained by a scatterometer,” *J. Ge.*, vol. 94, no. C7, pp. 9743–9759, 1989.
- [16] A. Stoffelen and D. Anderson, “Scatterometer Data Interpretation: Measurement Space and Inversion,” *J. Atmos. Ocean. Technol.*, vol. 14, no. 6, pp. 1298–1313, 1997.
- [17] J. Vogelzang, “Two-dimensional variational ambiguity removal (2DVAR),” de Bilt, the Netherlands, 2013.
- [18] Z. Wang *et al.*, “An improved wind direction modulation for Ku-band geophysical model functions , based on ASCAT and SCATSAT-1 collocations Key Points.”
- [19] M. B. Rivas, J. De Kloe, and A. Stoffelen, “Study of an Objective Performance



- Measure for Spaceborne Wind Sensors,” de Bilt, the Netherlands, 2009.
- [20] W. T. Liu, W. Tang, and X. Xie, “wind power distribution over the ocean,” *Geophys. Res. Lett.*, vol. 35, no. L13808, pp. 1–6, 2008.
 - [21] Z. Wang, A. Stoffelen, B. Zhang, Y. He, W. Lin, and X. Li, “Inconsistencies in scatterometer wind products based on ASCAT and OSCAT- 2 collocations,” *Remote Sens. Environ.*, vol. 225, no. February, pp. 207–216, 2019.
 - [22] A. Stoffelen and M. Portabella, “On Bayesian Scatterometer Wind Inversion,” *IEEE Trans. Geosci. Remote Sens.*, vol. 44, no. 6, pp. 1–11, 2006.
 - [23] J. Vogelzang, A. Stoffelen, R. D. Lindsley, A. Verhoef, and J. Verspeek, “The ASCAT 6.25-km wind product,” *IEEE J. Sel. Top. Appl. EARTH Obs. Remote Sens.*, vol. 10, no. 5, pp. 2321–2331, 2017.
 - [24] J. Vogelzang and A. Stoffelen, “ASCAT Ultrahigh-Resolution Wind Products on Optimized Grids,” *IEEE J. Sel. Top. Appl. EARTH Obs. Remote Sens.*, vol. 10, no. 5, pp. 2332–2339, 2017.